Accelerator measurements of the Askaryan effect in rock salt: A roadmap toward teraton underground neutrino detectors

P. W. Gorham,[1] D. Saltzberg,[2] R. C. Field,[3] E. Guillian,[1] R. Milinčić,[1] P. Miočinović,[1] D. Walz,[3] and D. Williams[2,*]

[1]*Dept. of Physics & Astronomy, University of Hawaii at Manoa, Honolulu, Hawaii, USA*
[2]*Dept. of Physics & Astronomy, University of California at Los Angeles, Los Angeles, California, USA*
[3]*Stanford Linear Accelerator Center, Stanford University, Menlo Park, California, USA*

We report on further SLAC measurements of the Askaryan effect: coherent radio emission from charge asymmetry in electromagnetic cascades. We used synthetic rock salt as the dielectric medium, with cascades produced by GeV bremsstrahlung photons at the Final Focus Test Beam. We extend our prior discovery measurements to a wider range of parameter space and explore the effect in a dielectric medium of great potential interest to large-scale ultra-high-energy neutrino detectors: rock salt (halite), which occurs naturally in high purity formations containing in many cases hundreds of km^3 of water-equivalent mass. We observed strong coherent pulsed radio emission over a frequency band from $0.2–15$ GHz. A grid of embedded dual-polarization antennas was used to confirm the high degree of linear polarization and track the change of direction of the electric-field vector with azimuth around the shower. Coherence was observed over 4 orders of magnitude of shower energy. The frequency dependence of the radiation was tested over 2 orders of magnitude of UHF and microwave frequencies. We have also made the first observations of coherent transition radiation from the Askaryan charge excess, and the result agrees well with theoretical predictions. Based on these results we have performed a detailed and conservative simulation of a realistic GZK neutrino telescope array within a salt dome, and we find it capable of detecting 10 or more contained events per year from even the most conservative GZK neutrino models.

I. INTRODUCTION

It is now widely understood that the universe becomes largely opaque to photons above about 100 TeV due to pair production on the cosmic infrared and microwave background [1]. Stable charged baryons or leptons do not become magnetically rigid enough to propagate over intergalactic distances until their energies are so high that they also suffer significant losses through interactions with the cosmic microwave background , through the process first noted by Greisen, and Zatsepin and Kuzmin (GZK) in the early 1960s [2,3].

Extragalactic astronomy in the 10^{15-21} eV energy range at ≥ 0.1 Gpc scales must therefore utilize other messengers, and neutrinos are the most likely contender. Moreover, the existence of sources that can produce single particles with energies approaching 1 Zeta-electron-volt (10^{21} eV $= 1$ ZeV $\simeq 60$ Joules) provides a compelling driver toward development of ultra-high-energy neutrino detectors, which can shed light not only on acceleration processes at the sources that produce the primary cosmic rays, but on the acute problem of their propagation and attenuation in the intergalactic medium through the GZK process. This process itself yields neutrinos as secondaries of the $p\gamma_{2.7K}$ interactions, a process first noted by Berezinsky and Zatsepin [4] and Stecker [4]. The resulting GZK neutrino spectrum, peaking at EeV energies [5], distinctly reflects the cosmic-ray source spectrum and distribution and provides unique diagnostics on the evolutionary history of the cosmic-ray accelerators.

Because the GZK neutrino flux arises from the aggregate intensity of all cosmic ray sources at all epochs, it is also potentially the strongest source of EeV neutrinos integrated over the entire sky, and may in fact act as a "standard test beam" for EeV neutrinos. At the low end of the GZK neutrino spectrum at 0.1 EeV (10^{17} eV), the center-of-momentum (CM) energy of GZK neutrino interactions on nucleons at Earth is 14 TeV, equaling that of the planned Large Hadron Collider. At the highest energies where the flux is still accessible, at several times 10^{19} eV, the CM energies are of order 250 TeV, well beyond what can be envisioned for any earth-based accelerator. Thus the possibility of high-energy physics applications which can test weak interaction models well beyond the currently accessible range cannot be ignored. The wide agreement for various flux models, combined with a strong science motivation from both particle physics and astrophysics, has made the detection of GZK neutrinos the focus of significant attention for all current high-energy neutrino detectors.

This goal compels us to consider detectors with target masses approaching 10^{42} nucleons, a teraton of mass, or 1000 km^3 water-equivalent at EeV energies [6]. Such a target mass must be physically accessible, and must be able to transmit information about embedded neutrino cascades within its enormous volume to a suitable and cost-effective detector array. A promising approach toward this daunting task is to utilize the Askaryan effect [7,8], a process which leads to strong, coherent radio pulses from

---

*Present address: Pennsylvania State University, State College, Pennsylvania, USA

such cascades. Several known dielectric media, with ice and rock salt the most promising at present, appear to have the necessary characteristics. Antarctic ice has been the focus of studies for this goal for several years now via the Radio Ice Cerenkov Experiment (RICE) [9], and the Antarctic Impulsive Transient Antenna (ANITA) long-duration balloon project will seek to exploit the effect in a novel approach [10]. A recent limit at extremely high neutrino energies has been reported via FORTE satellite observations of the Greenland ice sheet [11]. There is also another class of experiments searching for Čerenkov emission from ultra-high energy (UHE) neutrinos via neutrino interactions with the lunar regolith [12–15].

Rock salt, first suggested as a possible target medium by Askaryan [7], has also been the focus of recent efforts, and it appears to show significant promise in regard to potential for detector development, along with the potential advantage of greater accessibility [16,17] compared to Antarctic ice. We report here on experiments to further understand aspects of the Askaryan process with a particular focus on rock salt as the medium for the cascades and radio pulse production.

In our initial measurements of the Askaryan effect using a silica sand target [18], the total equivalent beam energy was varied from about 3×10^{17} eV to about 10^{19} eV, and radio measurements were made primarily in a 0.8 GHz band centered at 2.2 GHz, with some additional data at discrete frequencies. Polarization was measured at one
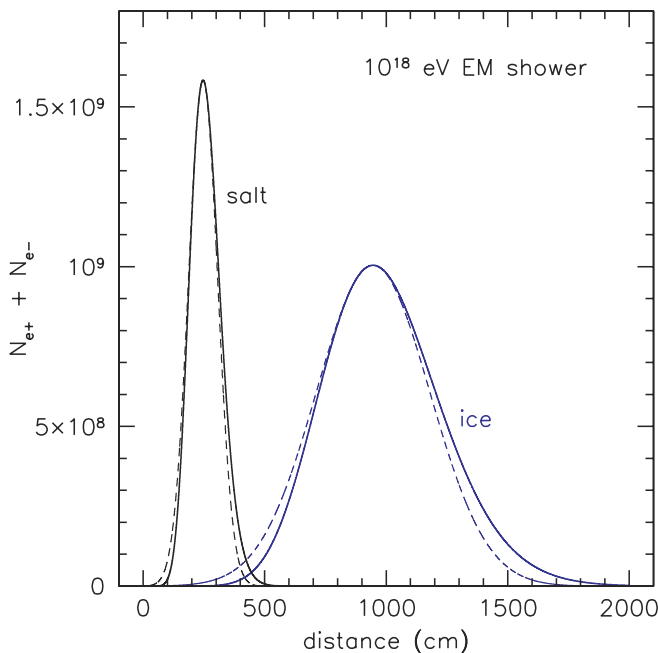

FIG. 1 (color online). Longitudinal shower profiles for two media, salt and ice now in use for radio detection of high-energy neutrinos. The solid curves are for the NKG approximation, and the dashed curves are Gaussian approximations to the NKG curves, used for parametrization of the emission (see text).

location external to the sand target. In this report, we verify the effect as expected for rock salt, and have extended the energy range of the measurements another 2 orders of magnitude down to 10^{15} eV. We have made measurements over a continuous radio and microwave frequency range from 0.2 to 18 GHz, and we have mapped the polarization of the emission at 21 locations along the shower. We have also made the first measurements of the coherent *transition radiation* from the Askaryan excess charge in a shower.

Our results now extend measurements of the effect over the entire range of cascade energies and radio frequency range of interest for GZK neutrino detection. We have also explored in greater detail the shower calorimetry aspects of radio Čerenkov measurements, and have made the first measurements of the vector change of polarization at different locations around the shower axis. This latter property, in particular, is unique to radio Čerenkov detection, and the combination of all these results gives us confidence that the approach to teraton neutrino detectors is still wide open using these methods.

Before describing the experiment and results, we include here a brief review of the characteristics of the Askaryan effect and the radiation it produces, and the general implications for its use as a detection method.

A. Background on Askaryan effect

In an electromagnetic cascade, particles with energies above the medium-dependent critical energy E_{crit} lose their energy primarily through pair production, bremsstrahlung, Compton scattering, and photonuclear processes, all of which lead to multiplicative growth in the total number of particles, until the mean particle energy falls below E_{crit} where ionization losses exceed those of the processes noted above. Several of these processes are asymmetric in their matter-antimatter response, for example, positrons can annihilate after production, and Compton up-scattering of electrons in the dielectric medium by photons leads to a larger number of high-energy electrons compared to positrons. Askaryan theorized that these processes lead to a net negative charge excess $N_{\text{excess}} = N_{e^+} - N_{e^-}$ in the electromagnetic shower, and he conservatively estimated it to be 10% of the total number of electrons and positrons combined (more recent estimates and detailed simulations give typical values of double this amount).

1. Coherence and shower properties

In dielectrics of typical solid densities ($\rho = 0.5$–2.5 gm cm^{-3}) the transverse and longitudinal dimensions of the charged-particle bunch comprising the shower are compact, several cm or less. At radio wavelengths λ longer than several times these dimensions, radiation produced by the bunch is completely in phase, or coherent, and the charge excess appears operationally as a single unit charge $Q = N_{\text{excess}} \times e$. For such radio wavelengths, the Čerenkov energy arrives as a single impulse, unresolved in

time, and therefore taking its shape from the intrinsic impulse response of the antenna and receiver. Such a signal is known as a *band-limited* signal. At wavelengths approaching the shower bunch dimensions, the impulse may begin to be resolved; this occurs at frequencies of several GHz or more, well into the microwave regime.

To first order, the number of charged particles at the maximum of shower development is $N_{tot} = E_{sh}/1$ GeV. The implied charge excess is thus $Q_{excess} \simeq 0.2 \times E_{sh}/1$ GeV. For a shower of $E_{sh} = 10^{18}$ eV, $Q \simeq 2 \times 10^8$.

The propagation distance over which the particle number exceeds half of its maximum value is of order 1.5 m in salt (or 5.5 m in ice) for this shower energy. An example of shower development in the total number of particles for two media of interest, salt and ice, is shown in Fig. 1, where the shower profile has been estimated through use of the Nishimura-Kamata-Greisen (NKG) parametrization [19]. The difference in development of the two showers is due primarily to the density, critical energy, and radiation length differences. For salt, the density is almost 2.5 times greater than ice, and E_{crit} (which depends on atomic and nuclear properties of the material) is 40% lower. The radiation length is nearly a factor of 4 lower than for ice. The net result of these effects is that a shower in salt grows and decays over a much shorter distance, and the lower critical energy means that it grows to a larger net total number of particles than for ice, since the shower growth can continue to a lower mean particle energy. Although not shown here, the transverse dimensions of the shower bunch are also more compact, leading to a higher degree of radio-frequency coherence.

2. Field-strength and angular distributions

The dashed curves in Fig. 1 indicate a fitted Gaussian profile for the shower development, which provides a convenient way to get a good first-order estimate of the Čerenkov power and angular distribution in the far-field. In the radiation frequency limit where full coherence obtains, given by the requirement that $kL \gg 1$, where the wave-number $k = 2\pi n\nu/c$ for frequency ν and index of refraction n, the field strength $(Vm^{-1}Hz^{-1})$ can be approximated as [11]:

$$|\mathbf{E}(\nu)| = \sqrt{2\pi}\frac{\mu\mu_0 QL\nu}{R}\sin\theta\, e^{-(kL)^2(\cos\theta - 1/n)^2/2} \quad (1)$$

where for typical dielectrics $\mu = 1$, $\mu_0 = 4\pi \times 10^{-7}$ is the permeability of free space, L is the parameter determined from the Gaussian fit of $q(z) = Q\exp(-(z - z_{max})^2/2L^2)$ to the shower profile with maximum at z_{max}, θ is the polar angle around the shower axis, and R is the distance to the shower. For the two showers shown above, $L_{ice} = 2.33$ m, and $L_{salt} = 0.60$ m (but these are of course energy-dependent because the shower length is energy-dependent).
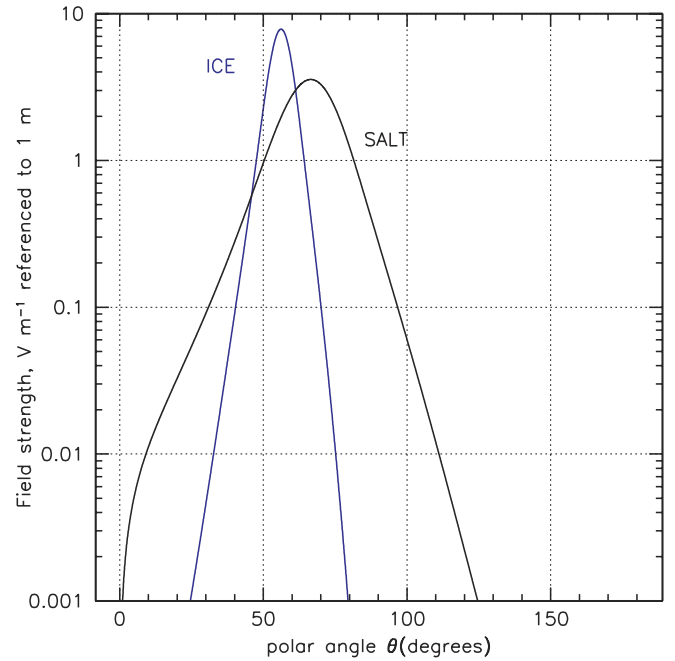

FIG. 2 (color online). Čerenkov angular distributions for the two showers given in Fig. 1 above.

Equation (1) can be integrated over a range of frequencies to give an estimate of the effective "beam pattern" that a shower will produce in the two media noted above for a typical broadband application. In Fig. 2 we show the result of such an integration over a bandwidth of 200 MHz, centered on 200 MHz, for a 10^{18} eV shower as shown above. The reduction in overall charged-particle track-length gives a reduction of the peak electric field strength in salt by about a factor of 2 as compared to ice. The angular emission is however much broader: at 10° off the Čerenkov angle, the emission field strength in ice is at less than 10% of its peak value; in salt at the same off-cone angle the field is still at 50% of its peak value. Such
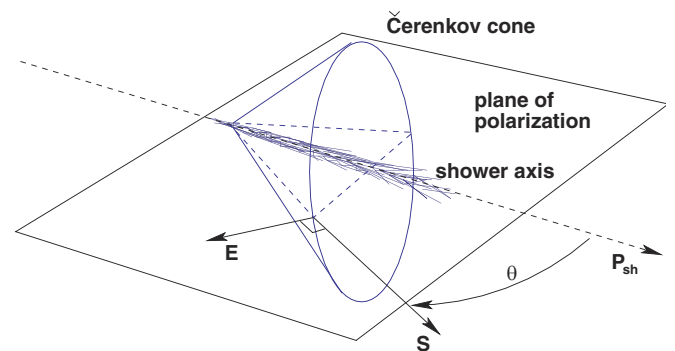

FIG. 3 (color online). Čerenkov polarization diagram. The plane of polarization contains the shower momentum vector $\mathbf{P_{sh}}$, the radiation Poynting vector $\mathbf{S}$, and the Čerenkov Electric field vector $\mathbf{E}$.

behavior leads to a larger detection solid angle for showers, but at a higher threshold energy.

3. Polarization

Čerenkov radiation theory requires that the emission be 100% linearly polarized, with the polarization lying in the plane containing the particle track and the Poynting vector of the radiation (Fig. 3), that is, the polarization unit vector $\hat{\mathbf{e}}$ must satisfy

$$\hat{\mathbf{e}} = \hat{\mathbf{s}} \otimes (\hat{\mathbf{p}}_{sh} \otimes \hat{\mathbf{s}}) \qquad (2)$$

where $\hat{\mathbf{p}}_{sh}$ is the shower momentum unit vector, and $\hat{\mathbf{s}}$ is the radiation Poynting unit vector. In optical ring-imaging Čerenkov counter applications, polarization is not typically used, since it is more difficult to measure the plane of polarization with incoherent intensity-based detection of the radiation. For radio detection, in which field-strength measurements can be made directly in orthogonal polarizations, such measurements are more straightforward, and data from our initial SLAC experiment [18] has already given clear evidence that such polarization characteristics obtain fully for the coherent radio emission resulting from the Askaryan effect.

Because one can combine knowledge of the direction of the Poynting vector (for example, from establishing the vertex of the radiation via geometric timing constraints from four antennas at different locations) with the measurement of the plane of polarization at each antenna to uniquely determine the direction of the particle shower, exploring the use of polarization information in detectors which exploit the Askaryan effect is of great interest for sky-mapping of neutrino sources. Thus we have paid par-
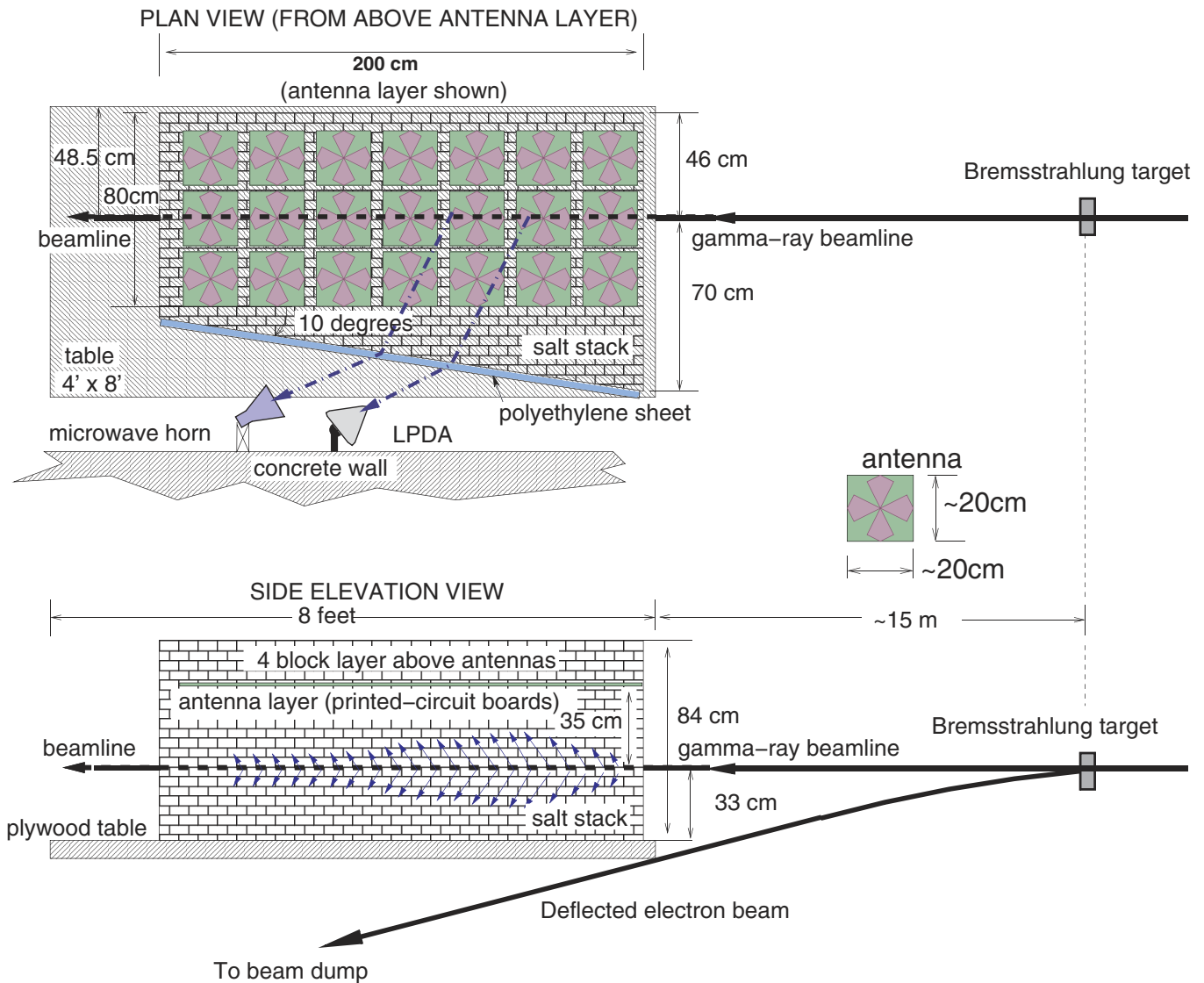

FIG. 4 (color online).   Geometry of the salt-block shower target used in the experiment.

ticular attention to polarization measurements and their relation to shower geometry in this report.

4. High-energy shower extrapolation

The showers produced in our experiments consist of the superposition of a large number of GeV electromagnetic cascades, with energies that sum up to EeV levels, but whose development is determined by the convolution of a GeV cascade and the exponential first-interaction distribution of the input photons. As such it cannot simulate the leading interactions of a cascade initiated by a single high-energy particle, either in the longitudinal shower distributions of particle number, or in the exact particle species content. However, these differences are of little consequence for radio production, since the Askaryan emission is dominated by the electron excess at energies below ~ 100 MeV, near the region of shower maximum. The charge excess itself is quite similar in either case, and the main quantitative differences come in only as the logarithm of the ratio of the lead particle energy to the critical energy, which produces a more extended shower maximum region in the case of a shower initiated by a high-energy particle, and gives more total track-length for Cherenkov production. These differences are easily quantified by standard shower theory, and in practice the GeV composite showers used here can be used to rigorously test models for the Askaryan radio emission.

II. EXPERIMENTAL SETUP

The experiment (SLAC T460) was performed at the Final Focus Test Beam (FFTB) facility at SLAC in June 2002. As in our first SLAC measurement [18], we used gamma-rays from a series of Aluminum radiators of different thicknesses to provide secondary bremsstrahlung gamma-rays for shower production in our rock salt target. The geometry of the target is shown in Fig. 4. It was built of 1.8 kg salt bricks obtained from Morton Salt Inc., with a total mass of about 4 metric tons. The bricks are slightly trapezoidal in all of their cross sections to accommodate the manufacturer's mold release, but have average dimensions of $15 \times 10 \times 6$ cm. Such bricks are food-grade, and specified to be at least 99.5% pure sodium chloride. They are manufactured by compression molding of crystalline salt under ~ 450 tons per in^2 pressure. Their density was measured to be 2.08 g cm^{-3}, which is about 3% less than the density of pure halite mineral.

Measurements of the water content of small samples of a typical brick found only trace amounts of volatiles (including water), below 0.17%. Laboratory measurements of sodium chloride crystals at comparable purities give upper limits of $\leq 10^{-4}$ on the loss tangent $\tan\delta$, which is related to the absorption coefficient α, for small values of $\tan\delta$, by

$$\alpha \simeq \frac{2\pi\nu}{c}\sqrt{\epsilon}\tan\delta(m^{-1})$$

for frequency ν, real part ϵ of the dielectric permittivity, and speed of light c. The implied upper limits on the attenuation length $L_\alpha = \alpha^{-1}$ are hundreds of meters [20] in the UHF and cm wave regime, and our tests through of order $0.3 - 0.4$ m of the salt bricks found no measurable attenuation. In the results reported here we assume negligible bulk absorption of the radio emission. Paper labels attached to the the top of the bricks were found to be difficult to remove, and after we confirmed that the labels were nonconductive and had no effect on the radio transmission, they were left alone.

To minimize the effects of the slight gaps left when stacking the salt blocks, pure (food-grade) uniodized table salt was used to fill in the interstices. A 2.5 cm thick polyethylene sheet was also mounted along the Cherenkov radiator surface to provide a smooth refracting surface for the external antennas and some improvement in index matching because of the intermediate radio frequency (RF) index of refraction of polyethylene.

An array of 7 by 3 (21 total) printed-circuit board broadband dual-linear-polarization bowtie antennas was embedded in the upper portion of the target, on a rectangular grid with spacings of 22 cm along the shower axis and 21 cm transverse to it, with one set of antennas arranged with one of their polarization axes aligned directly above the beamline. These are shown schematically in Fig. 4. The antennas had a frequency response of ap-

FIG. 5. View of the salt stack construction at the antenna layer. Antennas were mounted with their leads passing through drilled salt blocks as seen in several examples on the top of the stack.

proximately 0.2–2 GHz, and about −12 dB of cross-polarization rejection.

In addition to the embedded array, we also used two external antennas, a C/X-band standard gain horn usable over the frequency range from 5 to 9 GHz, at a fixed location on the side of the target; and a 1–18 GHz log-periodic dipole array (LPDA) antenna with a single linear polarization, which was also located to the side of the target but could be repositioned. One side of the salt stack was arranged with a 10° angle with respect to the beamline to facilitate transmission of the Čerenkov radiation, which would have otherwise been totally internally reflected from a parallel face. The partially constructed salt stack is shown in Fig. 5 at the antenna layer, with several of the antennas evident, assembled with their leads projecting through a drilled salt brick.

All antenna signals were digitized with Tektronix digital oscilloscopes (a TDS694C 3 GHz bandwidth, 10 Gsamples/s; and a CSA8000 sampling scope, 20 GHz, up to 100 Gsamples/s) using an ultrastable microwave transition-radiation-based trigger from an upstream location. Runs were also taken with the bremsstrahlung radiators in and out of the beam at numerous times during the data collection to test for the presence of accelerator backgrounds, which were found to be negligible. The total shower energy was varied by changing both the electron beam intensity and the thickness of the bremsstrahlung radiators. These radiators varied from 0.06% to 1.5% of a radiation length (RL) and thus extracted the same fraction of the electron beam energy in bremsstrahlung photons. The electrons were then steered away from the salt target and dumped into the FFTB beam dump approximately 20 m downstream. The bremsstrahlung photon spectrum from the radiators used is very broad with a mean energy of several GeV.

SLAC beam current monitors allowed us to reduce beam intensity to about 10^9 electrons per bunch using conventional methods. Below this level, closed loop control (eg. fine-tuning) of the beam direction was not possible. However, by employing our high signal-to-noise coherent microwave transition radiation trigger, we were able to further monitor the beam intensity to levels an additional 2 orders of magnitude below this. With the combination of radiators available to us, the dynamic range of the showers obtained was thus about 4 orders of magnitude in shower energy. The excellent stability of the FFTB beam assured that no retuning was necessary during our measurements, which were repeatable once the beam intensity was set back to the higher levels again.

III. RESULTS

To provide a baseline for evaluation of the results, we simulated the electromagnetic showers using the Electron Gamma Shower 4 (EGS4) Monte Carlo code [21]. EGS4 cannot directly simulate the radio emission from the show-
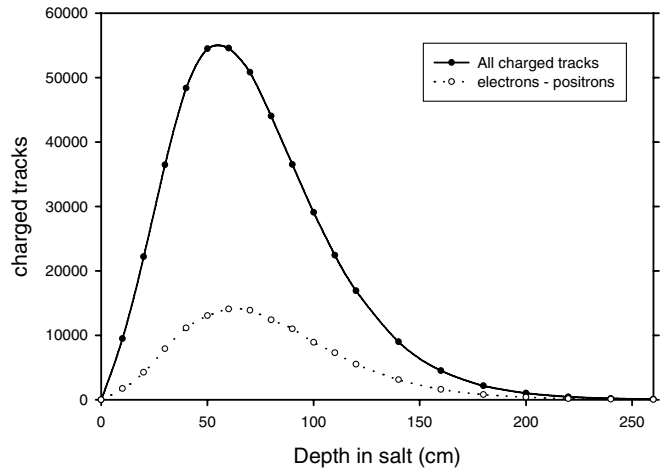

FIG. 6. Longitudinal distribution of the bremsstrahlung shower, for both total charge and charge excess as simulated by EGS4 for rock salt.

ers, but can assess both longitudinal and lateral development of the total charged particle and photon content of the shower, as well as the Askaryan charge excess.
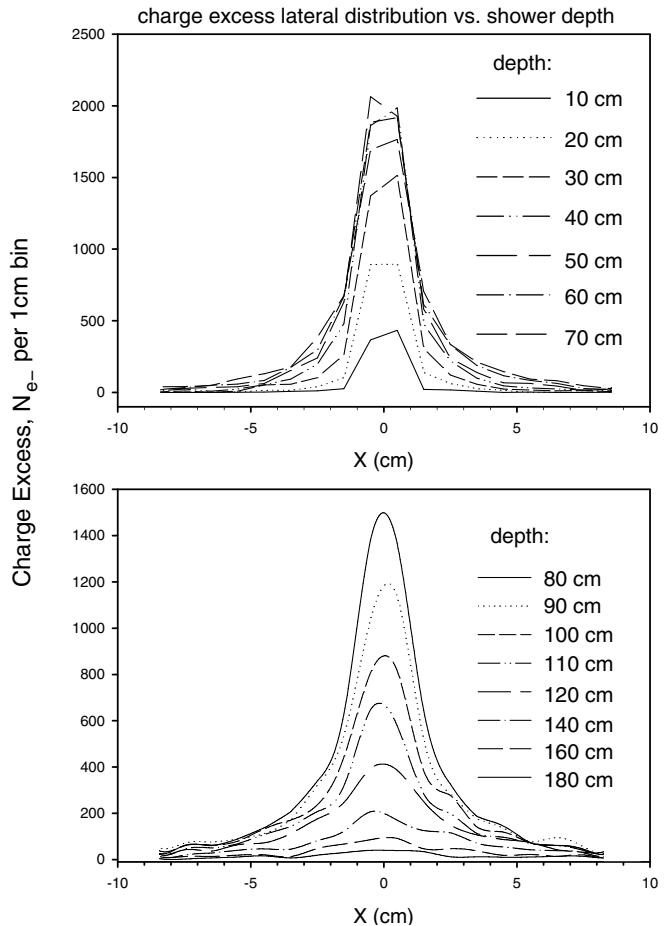

FIG. 7. Lateral distributions at various depths. Top: depths less than 70 cm. Bottom: depths greater than 70 cm.

FIG. 8.   The exit point of the beam in the downstream wall of the salt target, outlined by discoloration of the salt produced by beam and showing in cross section at the exit surface. Even at this location of order 15 radiation lengths along the shower, the shower core is still only several cm across (the salt blocks are 6 by 10 cm here in cross section).

Figure 6 shows the longitudinal shower development for a salt target, including the charge excess. Figure 7 shows a series of profiles of the shower lateral distribution of the excess charge at different depths in cm, indicated on the plot. In each case the simulation is for a thousand 28.5 GeV electrons initially, led through a 10% RL bremsstrahlung radiator to fully account for the secondary photon spectrum. No changes are required to the EGS4 code to develop the ~25% negative charge excess seen; this again demonstrates that the Askaryan effect is generic to electromagnetic showers.

The simulations of the shower transverse distribution were qualitatively confirmed by the appearance of a deposit of discolored material along a volume of salt within the stack during the experiment, the evidence of which is shown in Fig. 8. The size and shape of this cross section of the contaminated region is an indication of the size of the shower core itself, and it is still of order several cm in diameter even at a depth of ~15 radiation lengths.

A. Coherence and absolute field strength

In reference [18], the coherence of the radiation was observed over a fairly limited range of shower energies, from about 3×10^{17} eV to 10^{19} eV composite energy. In our current measurements, we have extended the coherence measurements to a much larger range. These measurements were made using averaged results from several of the bowtie antennas around the region of shower maximum. Typical runs at a given total charge per bunch (which
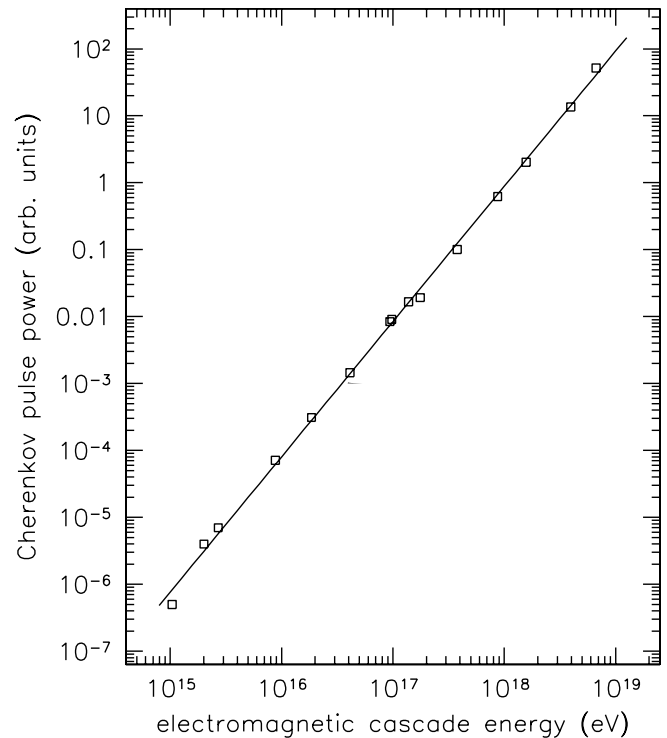

FIG. 9.   Observed coherence of the 0.3–1.5 GHz radiation as a function of total beam energy per pulse. The curve shows a quadratic relation for power as a function of shower energy, and the points are the measured data.

determines the composite energy per bunch) were averages of 1000 beam shots, and the beam current was separately monitored for stability. Typically we also recorded 100–1000 shot-to-shot pulse profiles to monitor the variance. Once corrected for minor variations in beam current, these were stable to the level of a few percent.

Figure 9 shows the results of the relative radio-frequency power as a function of shower energy, now covering nearly 4 orders of magnitude in energy and 8 orders of magnitude in RF power. No departures from the expected quadratic dependence of pulse power with shower energy are seen. This result demonstrates the remarkable dynamic range possible for detection of coherent RF Čerenkov radiation.

Determination of the absolute measured field strength of the showers requires that the antenna effective area, spectral response, coupling efficiency, and angular response all be included in converting the measured voltages to field strengths in the detection medium. To properly account for the angular response, one must first determine if the conditions for the reception are near-field (Fresnel zone) or far-field (Fraunhofer Zone) for both the antenna and radiation source. The conditions for far-field response are approximately

$$f \leq \frac{Rc}{L^2 \cos^2\theta} \qquad (3)$$

where R is the distance between source and antenna, L the

largest antenna dimension, θ angle of incidence with respect to the normal (broadside) of the antenna, and f is the highest frequency for which far-field conditions are met. For the antenna as a receiving component, with $R = 38$ cm, $L = 20$ cm, and $\theta = 25°$ at the Čerenkov angle the antenna far-field conditions are satisfied for frequencies below 2 GHz, the highest usable frequency for the bowtie antennas.

While the shower is in the far-field of the antenna, the converse is not the case, since the radiation develops over a region comparable in size to the entire shower with a length of about 80 cm for full-width-at-half-maximum near the peak of cascade particle development. In practice this means that while the far-field antenna beam patterns may be used to determine the bowtie amplitude response with angle, they receive radiation only from approximately that portion of the shower that is projected onto the antenna effective area at the Čerenkov angle (about 66°). This behavior was observed in Ref. [18], and provides the possibility of tracing out the longitudinal charge evolution of the shower by measuring the change in radiation amplitude along the shower axis, as was done in Ref. [18] (see

also Fig. 14 below). In determining the absolute field strength one must therefore account for the fact that the shower is effectively resolved into these individual sections.

Figure 10 (top) shows a plot of the summed field strengths from all of the bowtie antennas, corrected for known cable attenuation but not for other frequency dependent effects. The pulse shape is typical of the impulse response for bowtie antennas, and no attempt at deconvolution of the intrinsic pulse has been made for these antennas, since the exact phase vs.. frequency was not known. In the bottom portion of the figure, a Fourier amplitude spectrum of the field strength is shown, including now corrections for the gain of the bowtie antennas, which can be done independent of the phase uncertainty. The solid histogram shows the power spectrum of the pulse, and the points are averages over 250 MHz sections of the spectrum, with the error bars based on the spectral variance within each section. It is evident that there are some near-nulls in the bowtie response, but the overall trend is for a rise at the higher frequencies, consistent with Čerenkov radiation.

In Fig. 11 (top), we show the results of deconvolution of the data obtained using the full bandwidth (0.8–18 GHz) of the log-periodic dipole array antenna. Here we have corrected for the measured amplitude and phase response of both the antenna and cable. The nearly antisymmetric
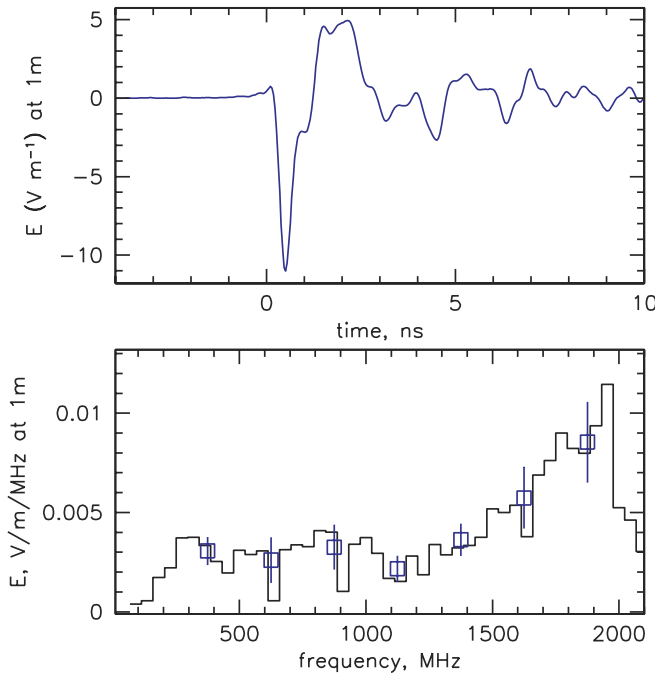

FIG. 10 (color online). Top: Summed-in-phase pulse profile from all bowtie antennas, with only cable attenuation amplitude corrections applied. Antenna angular response corrections are not applied here due to unknown phase corrections. The antenna is also in the near-field of the shower, and thus only receives a portion of the total shower radiation. Bottom: Power spectrum of the bowtie data, corrected for cable attenuation as in the time domain case above, and also amplitude-corrected for antenna angular response. No correction is applied here for the near-field effects of the shower. Points are averages over 250 MHz portions of the spectrum, with standard errors from the bin variance.
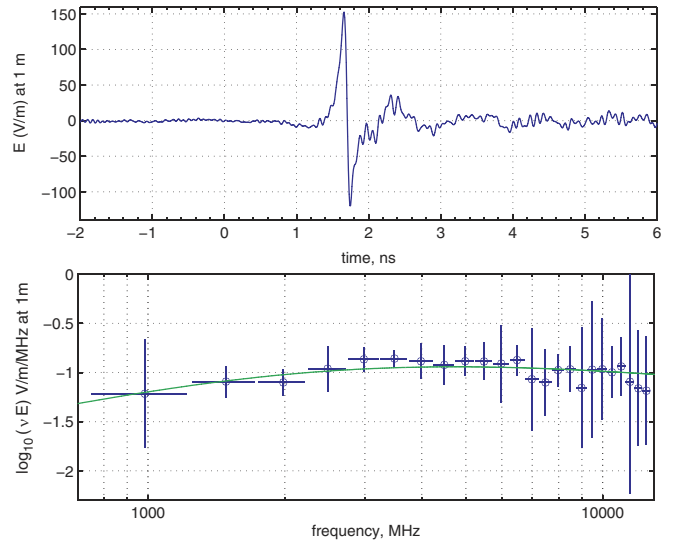

FIG. 11 (color online). Top: The intrinsic Askaryan pulse shape derived for the frequency range from 0.8 to 12 GHz, based on deconvolution of the LPDA data. The full-width at half-maximum of the initial pulse is about 60 ps. Bottom: Electric-field amplitude spectrum of the deconvolved pulse shown in the top pane, multiplied by frequency ν which accounts for first-order near-field effects. Horizontal bars indicate the range of the frequency bins used; vertical bars indicate the standard deviation of the spectral data within a bin. The curve shows a comparison to a standard model for the spectrum [22–24].

bipolarity of the pulse appears to be fundamental to the pulse-forming mechanism itself, and gives an extremely sharp pulse with spectral components extending to about 12 GHz in our measurements. The spectrum extends beyond 12 GHz but the cutoff in our data is due to loss of signal-to-noise due primarily to cable attenuation.

In Fig. 11 (bottom), the derived amplitude spectrum of the pulse shown in the top pane is shown, with a first-order correction for near-field effects applied so that the spectral response can be compared to the frequency dependence of the model in references [22–24]. The correction consists of a simple scaling of the field linearly with frequency, that is $\mathbf{E} \rightarrow \nu\mathbf{E}$. The motivation for this correction is that the width of the Čerenkov cone decreases as $1/\nu$ [22–24], thus leading to a similar near-field decrease in the region along the shower which can contribute radiation to the receiving antenna. Once this effect is compensated for, there is good agreement with the theoretical expectations.

We also measured the coherence at microwave frequencies (2.2–18.0 GHz) in several bandpasses, using the LPDA and the C/X-band horn antennas, both of which had known effective areas. Figure 12 shows the measured electri -field strength vs. total shower energy at different frequencies. Measurements were done with the LPDA in bands centered on 4.95 and 14.5 GHz, respectively; and with the horn antenna at 7.4 GHz, with bandwidths of about ± 1 GHz. Points represent measured values and lines are least-square fit curves $|\mathbf{E}| = AE_{\text{sh}}{}^{\alpha}$, where $\mathbf{E}$ is the electric field and E_{sh} the shower energy. The fit for the exponent α gives: $\alpha_{4.95} = 1.00 \pm 0.04$ at 4.95 GHz, $\alpha_{14.5} =$
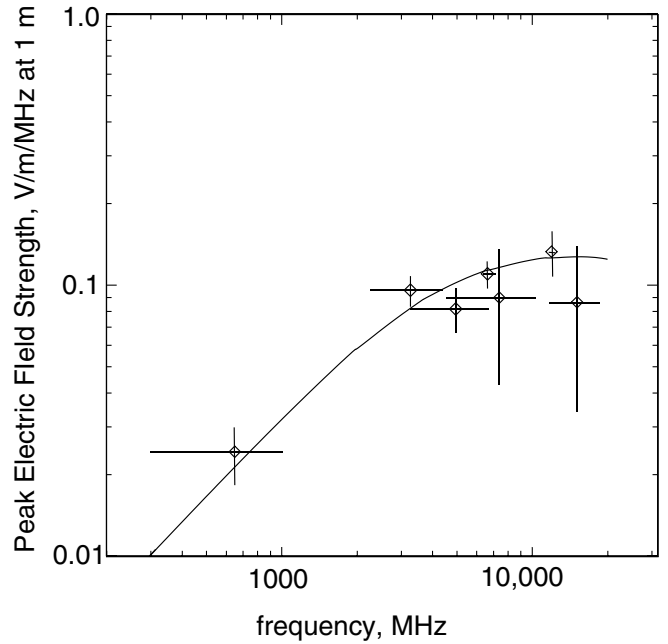
FIG. 13. Spectral dependence of the measured electric field strength for shower energy 1.9×10^{18} eV. The solid curve is a parametrized Monte Carlo simulation scaled for synthetic rock salt. Vertical bars are estimated errors, largely due to systematics in the absolute RF calibration; horizontal bars indicate the bandwidth used.

1.02 ± 0.11 at 14.5 GHz, $\alpha_{7.4} = 0.99 \pm 0.05$ at 7.4 GHz. At all three frequencies, the field strength is in agreement with full coherence of the radiation.

To compare the absolute power levels of the filter-banded data with the theory, we corrected for both near-field, beamwidth, and shower profile effects. Figure 13 shows the absolute field strength measured in several frequency bands from 0.3–15.0 GHz. The plotted curve is based on the parametrization given in [22,23], scaling from ice to synthetic rock salt (for details see Appendix B). The horizontal bars are not standard errors but show antenna or filter bandwidth, and vertical bars indicate combined statistical and systematic uncertainties. The measured spectrum of the pulse electric field is in good agreement with the prediction.

B. Polarization and charge excess tracking

The crossed bowtie antennas employed in our measurements provided simultaneous measurements of the induced voltage in orthogonal linear polarizations, but because of their geometry, there is inherent leakage of a copolarized signal into the cross-polarized receiver. With a measured 14 dB of cross-polarized rejection, up to 20% of the copolarized amplitude (eg. voltage) can appear in the cross-polarized channel. To make accurate estimates of the angle of the projected plane of polarization of the radiation, the polarization leakage must be accounted for. We use a simple model for this, where the co- and cross-
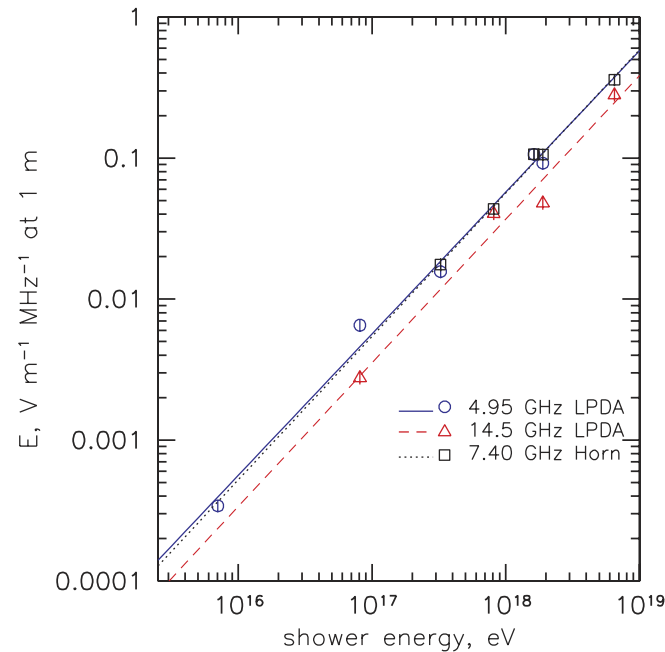

FIG. 12 (color online). Measured coherence of electric field strength at 4.95, 14.5 with LPDA and 7.4 GHz with horn antennas, respectively, with least-squares fit curve.

polarized voltages are related by:

$$V_0 = \mathbf{E} \cdot [\mathbf{h_0} + \alpha \mathbf{h_{90}}] \qquad (4)$$

$$V_{90} = \mathbf{E} \cdot [\mathbf{h_{90}} + \alpha \mathbf{h_0}] \qquad (5)$$

where $\mathbf{E}$ is the electric-field vector of the radiation and $\mathbf{h_{0,90}}$ are the vector effective heights (which are complex in general) of the co- and cross-polarized antennas. Since each of the bowtie antennas are identical in both the co- and cross-polarized directions, and since the induced voltage has a simple sinusoidal dependence on the projected plane of polarization angle Ψ (assuming no net circular polarization), we can write

$$V_0 = Eh(\cos\Psi + \alpha \sin\Psi) \qquad (6)$$

$$V_{90} = Eh(\sin\Psi + \alpha \cos\Psi) \qquad (7)$$

where $h = \frac{1}{2}(|h_0| + |h_{90}|)$ has the same magnitude for both the co- and cross-polarized antennas.

In our case we choose the copolarized direction to be aligned with the beam axis, since the radiation is naturally expected to be polarized along this axis. If we assume that Ψ is approximately aligned with the beam axis (in practice this was done to a precision of about $1 - 2°$, then for an antenna along the beam axis, we find to a good approxi-

mation that $\alpha = (V_{90}/V_0)|_{\text{on-axis}}$. Ψ is then determined by

$$\Psi = -\tan^{-1}\left(\frac{\alpha - V_{90}/V_0}{\alpha V_{90}/V_0 - 1}\right). \qquad (8)$$

Figure 14 shows results of the polarization and relative amplitude measurements for all 21 of the bowtie antennas. The top pane plots these as vectors with scaled lengths and directions corresponding to the square root of the amplitude (used for clarity for the lower amplitudes) and the projected plane of the polarization Ψ. In the lower pane of the figure, we also show the relative amplitude of the antennas along the center axis as a function of the longitudinal distance along the shower (corrected for the Čerenkov angle projection). We also plot the EGS4 simulation of the shape of the charge excess along the shower (about 27% of the total charge). There is excellent agreement between the measured shape of the amplitude response and the normalized charge excess predictions from EGS4.

In Fig. 15 we show similar data for the three antennas at shower maximum at a depth of 50 cm, now plotting the plane of polarization as a function of the transverse position of the antenna with respect to the centerline of the beam. All of the antennas lay in a plane about 35 cm above the beamline. The solid curve shows the expected change in the angle of polarization for the three antennas, and the agreement is good.

C. Transition radiation

Transition radiation (TR) and Čerenkov radiation are closely related; this is particularly true in the radio regime, where both forms of radiation may coexist in partially or fully coherent forms, and interference between them may
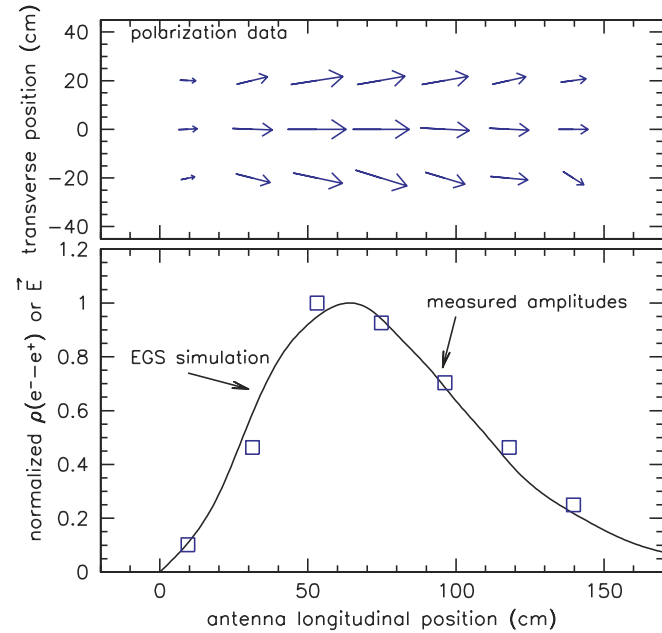

FIG. 14 (color online).   Top: Measured polarization vector field at the bowtie antenna locations in a plane 34 cm above the shower axis. The antenna feed center locations in that plane give the base of each vector, which is scaled in length as the square root of amplitude for clarity. The angles of the vectors match the observed polarization angles. Bottom: The observed amplitude of the received RF pulses along the center line of the antenna array. Also plotted is a curve of an EGS simulation of these showers; both curves are normalized to unit peak amplitude.
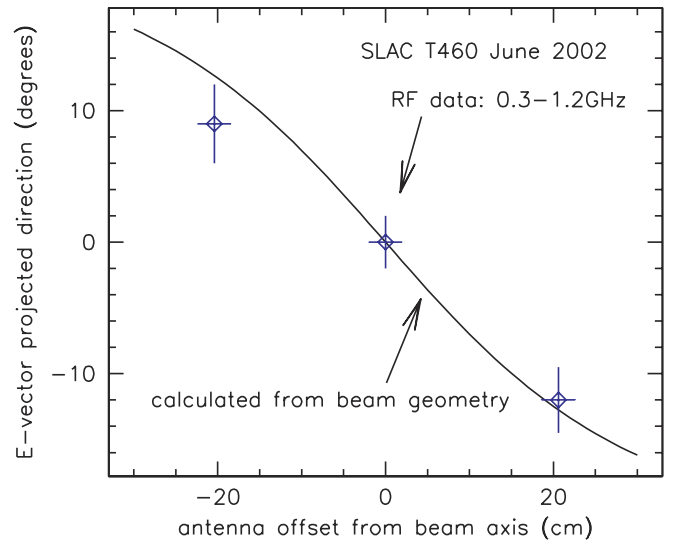

FIG. 15 (color online).   Plane of polarization vs. transverse distance of the antennas, which were all about 35 cm above the axis of the beam.
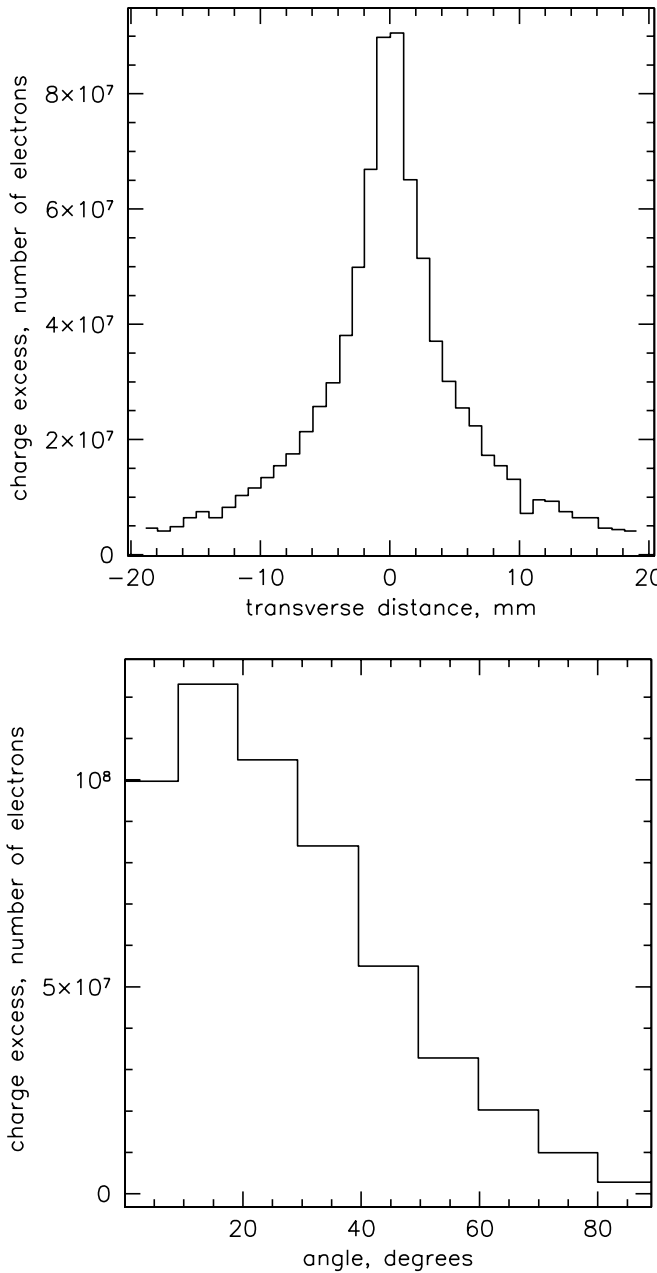
FIG. 16. Top: Transverse spread in the simulated electron shower emerging from the TR radiator, grouped in 1 mm annular bins around the beam axis. Bottom: angular emittance spread in the same electron shower, for the highest energy bin ($0.975 < \beta < 1$), in annular bins of solid angle, with 10° angular width.

result. In earlier work [25] we demonstrated the existence of free-space coherent microwave TR from relativistic electron bunches exiting an accelerator beam pipe, and confirmed the predicted angular dependence and polarization of the radiation. However, there was a serious discrepancy in these earlier measurements with regard to the total emitted power, which was observed to be significantly lower than predictions.

Transition radiation in the radio regime is of particular interest for detection of high-energy particle showers, since the Askaryan charge excess guarantees not only coherent Čerenkov radiation, but also TR when there is any change in the dielectric medium on scales comparable to the size of the shower. Showers which break through a solid surface can produce forward TR in the direction of propagation, and showers originating in one medium (air, for example) which then intersect a solid surface will produce backward TR which propagates opposite to the original shower direction. It is thus of some importance to establish the emitted power from this process, to determine under what circumstances it may be useful for high-energy shower detection.

In a setup that was independent of the salt target, and done after the work with the salt was complete, we used the photon beam to produce an electron-gamma shower in a 2 cm block of lead followed by a 1.3 cm block of aluminum. The excess electrons from the shower are thus expected to produce TR as they exit the aluminum. Strong RF pulses were observed with an X-band horn, with typical duration of 0.45 ns, consistent with a completely band-limited signal ($h_{\mathrm{eff}} = 2.4$ cm, $\langle \lambda \rangle = 4.2$ cm, $d\nu = 2$ GHz, effective area $A_{\mathrm{eff}} = 18.87$ cm^2). An EGS simulation provided us with an estimate of the number of excess electrons, their energy, and their angular and transverse distributions, which are shown in Fig. 16. In an appendix, we provide details of the calculation of the expected TR power, which depends on the geometric form factors of the exiting bunch. The transverse and angular divergence parameters are estimated to be $\sigma_T = 6$ mm and $\Omega = 30°$, respectively; therefore $f_T = 0.996$ and $\chi = 0.08$. Most of the shower electrons are in the highest energy bin ($0.975 < \beta < 1$), for simplicity we use only the electrons in that bin for this calculation, setting the average $\beta = .9875$. We assume the longitudinal form factor $f_L = 1$ which is reasonable given the very tight longitudinal distribution of SLAC bunches.

The results of the TR run are shown in Table I.

Here, the predicted power is about half the measured power, much closer than in our previous result [25]. The predicted electric field is 90% of the measured electric field. We would expect it to be about 70% of the measured electric field based on the factor of 2 difference in the power, but the electric field estimate assumes a perfectly triangular envelope, which is not accurate. Detailed studies indicate that the peak and RMS voltages are related by $V_{\mathrm{RMS}} = kV_p/2\sqrt{2}$, where $k \approx 1.4$ [26].

TABLE I. TR measurements and analysis.

θ	D cm	$d\Omega$ msr	N_e	P_L mW (calc.)	P_L mW (meas.)	E V/m (calc.)	E V/m (meas.)
10°	135.5	1.03	5.3×10^8	0.26	0.50	0.28	0.31

IV. DISCUSSION

Our measurements have extended the validity of the theory underlying the Askaryan effect to a second dielectric material, with 30% higher density compared to silica sand, and a 40% higher dielectric constant. In all cases the theory appears to scale as expected by the material properties, and there is no reason to believe this scaling would not apply for other dielectric materials as well. The measurements of transition radiation from the charge excess are the first observations of this effect, and lends further strength to the Askaryan hypothesis that a negative charge excess is responsible for the coherent radio emission, for if this were not the case, there is no obvious way to produce the measured transition radiation with the strength observed.

This latter effect could be important for both cosmic ray shower and neutrino shower detection, since there are many physical situations where a shower encounters a discontinuity of some kind that can lead to transition radiation. For example, ultra-high-energy air showers encountering clouds will see a dielectric discontinuity; and giant air showers which impact the earth or the surface of the ocean will certainly produce strong backward transition radiation, particularly in the latter case where the Fresnel reflection coefficient from the surface of the ocean is of order unity.

Our radio Čerenkov measurements demonstrate conclusively that coherent Čerenkov radio pulses from showers in the rock salt can accurately reconstruct the profile of the shower development as well as the total shower energy. They show that the process is inherently quadratic in the rise of power vs. shower energy, and this relationship is reliable over many decades of these parameters. Combining these results with *in situ* measurements of propagation characteristics at radio frequencies in salt domes [17] which indicate ≥ 250 m attenuation length, we conclude that nothing in principle prevents the development of embedded antenna arrays within large salt structures such as salt domes for the characterization of ultra-high-energy neutrino fluxes.

A. Application to detector modeling

To further understand how this technique might be applied, we have created a Monte-Carlo simulation of a large-scale antenna array embedded within a generic salt dome, where the halite with the highest purity is likely to reside. We denote the array here as a Salt dome Shower Array (SalSA). The array is cubic with 1728 antenna nodes ($12 \times 12 \times 12$), with a grid spacing of 225 m, of the same order as conservative *in situ* estimates [17] of the field attenuation length in rock salt, which we assume to be 250 m in this simulation. In fact recent laboratory measurements using a dielectric cavity [16] on samples of rock salt from the Hockley salt dome favor $L_\alpha \simeq 900$ m at

200 MHz, and similar long attenuation lengths are also favored by ground-penetrating radar data [17].

Each node consists of 12 closely spaced antennas (0.75 m vertical offset), 6 of which are dipoles with vertical polarization, and 6 of which are slotted-cylinder antennas which are sensitive to horizontal polarization. The antennas are both assumed to have $\cos^2\theta$ response functions for simplicity here. The assumption is accurate for fat dipoles or bicones in the vertical polarization [27]; for our slot cylinders, the response in practice is somewhat more flattened than $\cos^2\theta$ with a 1–2 dB front-to-back asymmetry, but we anticipate further development of current designs will tend to converge on a more uniform dipolar response.

Multiantenna local nodes such as this are effective in enabling a lower local-trigger threshold in the presence of Gaussian thermal noise, and are very cost-effective since the antenna elements themselves are inexpensive. The antennas are based on Numerical Electromagnetics (NEC2) models and actual tested prototypes, and are optimized for frequencies centered at about 20 MHz, with bandwidth of about 100%. Beam patterns for the midfrequencies are assumed.

A system temperature of 450K is assumed, based on about 310K for the salt and a receiver noise temperature of 140K, consistent with low-noise amplifiers that are readily available commercially. The basic design for node electronics centers on the use of a switched-capacitor array (SCA) transient digitizer, which is only read out and sent to the surface when the local node is triggered; a prototype of the basic design, which uses Gigabit ethernet on one fiber per node to the surface, is described by G. Varner *et al.* [28,29].

1. Hardware trigger rates

For triggering, an event must produce a voltage magnitude above 2.8σ on 5 of 12 of the local antennas within a node. This threshold and coincidence level is chosen both to reduce the accidental rates and to ensure a robust signal for reconstruction of the event. The accidental rates are addressed in the following discussion, and we note that the five 2.8σ signals yield a joint probability corresponding to 5.7σ, and even assuming one of the five is excluded for any reason, the remaining four signals have a joint 5σ probability.

The propagation time across the 9 m high node requires that the time window for such a coincidence be about 80 ns, corresponding to about 16 band-limited temporal modes of the antenna input noise voltages ($\tau = 1/\Delta f$). For these conditions, random coincidence rates per node per coincidence window are given by the cumulative binomial probability density function:

$$P(p, k, N_\tau) = \sum_{k}^{N_\tau} \frac{N_\tau!}{k!(N_\tau - k)!} p^k (1-p)^{N_\tau - k} \qquad (9)$$

where p the individual antenna probability of exceeding a

given voltage threshold in the window, k the number of antennas required above threshold, and $N_\tau = \frac{T}{\tau} N_{\text{ant}}$ is the product of the number of antennas N_{ant} and the number of independent temporal modes of length τ within a coincidence window. Since antenna noise voltages obey a nearly Gaussian voltage distribution [27]

$$p = \frac{2}{\sqrt{2\pi}} \int_{2.8}^{\infty} e^{-x^2/2} dx = 0.005\,11. \qquad (10)$$

For bandwidths of $\Delta f \simeq 200$ MHz, $\tau = 1/\Delta f \simeq 5$ ns, and thus the number of possible "cells" that can combine to form a node trigger is $N_\tau = 16 \times 12 = 192$. The resulting probability of a single node trigger per 80 ns is $P_{\text{node}} = 3.27 \times 10^{-3}$, yielding a node random trigger rate of about $R_{\text{node}} = 65$ kHz.

Since this rate is too high for sustained transient digitizer throughput, an additional digital signal processor is used to reduce the rate by first-order causality constraints. To enforce causality for the local antenna node triggers, we require that the hits along a node evolve along a proper light cone. Consider a matrix of 12 antennas by the 16 independent 5 ns temporal modes in the 80 ns coincidence window, giving a 192-cell array of antenna hits vs. time. Considering only plane waves for the moment, causality requires that hits evolve along the node on linear trajectories which must begin or end with the upper or lower antenna. There are ~16 upgoing and ~16 downgoing such trajectories, each of which has $P(p = 0.0511, k = 5, N_\tau = 12) = 2.67 \times 10^{-9}$ from Eq. (9). Any of the 32 causal trajectories can begin in each 5 ns temporal mode, so the random rate for such node triggers is

$$R_{\text{node}}^C \simeq 2.67 \times 10^{-9} \frac{32}{5 \times 10^{-9}} \simeq 20 \text{ Hz}$$

which provides ample margin on the expected ~1 kHz throughput of the transient digitizer, and allows for some relaxation of the trigger requirements to account for the additional possible patterns when wavefront curvature due to nearby showers is included.

Once these local node events are transmitted to the surface, global triggers based on array-processing of event clusters are determined. An example of how this may be implemented is as follows. For each array node that produces a trigger, we require a minimum of 4 additional local node triggers among all of its nearest neighbors including all diagonals. For each of the 8 array corner nodes there are 7 neighbors, for each of the 120 edge nodes there are 11, for each of the 600 face nodes there are 17, and for the remaining 1000 interior nodes there are 26. The light-crossing time in salt along the diagonal of an interior subcube of 27 nodes (consisting of a center node and its 26 neighbors) is 3.23 μs, or about 40 of the node trigger windows $T_{\text{node}} = 80$ ns. For a simple random coincidence, there are (27 nodes $\times$ 40 trigger windows) = 1080 cells in the trigger matrix. In this case, we use Eq. (9) with

$$p = P_{\text{node}} = T_{\text{node}} R_{\text{node}}^C = 80 \text{ ns} \times 20 \text{ Hz} = 1.6 \times 10^{-6}$$

along with k = 5, and N = 1080.

The resulting cluster trigger probability for the 3.23 μs window is $P_{\text{cluster}} = 1.27 \times 10^{-16}$, giving a net cluster trigger rate of $R_{\text{cluster}} = 3.9 \times 10^{-11}$ Hz. For the same 5-node criterion the corresponding probabilities and rates for the faces, edges, and corners are far lower. Thus the potential contamination of true events by random coincidences per year for the entire array is bounded by

$$R_{\text{array}} = P_{\text{cluster}} \times N_{\text{interior}} \times 365 \times 86400 = 1.23 \text{ Hz}.$$

indicating that, even prior to global event fitting constraints, the contamination from randoms can be made negligible. In practice, either local thresholds or cluster trigger criteria can be relaxed in hardware to ensure a manageable random "heartbeat" rate of order several Hz, and further constraints on cluster causality can be enforced in software. This will be done to ensure adequate real-time monitor of array instrument health.

2. Thermal noise backgrounds

From above, causality requirements alone are adequate to eliminate random triggers from the neutrino candidate event sample. The additional information from polarization, amplitude gradient, and antenna waveform phase at each node will only further establish this conclusion. The strength of these constraints arises primarily from the fact that each node is not just a point detector, but provides significant directional information on its own. The important conclusion here is that the sensitivity of our implementation is limited only by our conservative event reconstruction requirements (which determine the 5 antenna + 5 node coincidence levels), rather than random thermal noise backgrounds.

We stress that thermal noise backgrounds in radio Čerenkov detectors, while in some ways analogous to the through-going cosmic-ray muon backgrounds seen in lower-energy optical Čerenkov detectors such as AMANDA, are in fact quite distinct in practice, since they do not represent an irreducible background to the physics events, and cannot reproduce the characteristics of neutrino events. Atmospheric muon backgrounds in lower energy detectors are irreducible over some range of solid angle near or above the horizon. A more relevant comparison with thermal noise backgrounds can be made with downgoing muon events misreconstructed as upcoming neutrino-induced events in low-energy detectors. In this case, the frequency of misreconstructed events for the lower energy neutrino telescopes can be made negligible by choosing higher software thresholds, and the same is certainly true for radio detectors as well with regard to thermal noise backgrounds.

B. Simulation results

Figure 17 shows the dependence of the received voltage, based on the parametrization of reference [22,23], scaled for salt, as a function of distance and shower energy. The curves are labeled by shower energy in PeV, and both the 1σ and 2.8σ levels for RMS voltage above the baseline noise level are shown. The solid and dash-dot curves are for $L_\alpha = 250, 900$ m, respectively.

It is evident that the 225 m spacing we have employed in our Monte Carlo here will give a shower energy threshold in the neighborhood of 10 PeV for our baseline assumption of $L_\alpha = 250$ m, and in practice we find that other loss factors and the neutrino interaction Bjorken y-factor (e.g., inelasticity) contribute to push the optimal sensitivity to neutrino energies of order 30 PeV. Figure 17 indicates that, although it may be possible to operate a SalSA at a low enough energy threshold to detect events at the 6.4 PeV Glashow Resonance for W-vector boson production via $\nu_e + e^- \rightarrow W^-$, the node spacing required is below 100 m, implying an order of magnitude more array elements. Since, for a broad-spectrum neutrino source, the integral over the resonance is relatively small in terms of the number of events [30] compared to the continuum, the justification for the increased array density is not clear. In addition, the GZK neutrino spectrum peaks above $\sim$100 PeV. However, if $L_\alpha \gg 250$ m as indicated by re-

cent results, the energy threshold will be considerably lower, of order 10 PeV at a spacing of 225 m, and only a modest increase in array density required to achieve good sensitivity at the Glashow resonance.

The volume enclosed by our simulated full array is approximately 15.6 km^3 of salt, or about 34 km^3 water-equivalent (w.e.) mass. For the region within one attenuation length of the outer wall, for $L_\alpha = 250(900)$ m, an additional 11.4(63) km^3, giving 24.9(137) km^3 w.e. is contained where we have indicated the perimeter values for the longer attenuation length in parentheses. These perimeter events will in general also yield events which are well measured when they illuminate a portion of the face of the array. The effective fiducial volume thus approaches 60(170) km^3 w.e. for an array that easily fits into the upper $\sim$3 km of a typical salt dome. The solid angle acceptance of the array includes the entire upper 2π hemisphere, and extends up to $\sim$10° below the horizon, depending on neutrino energy. This implies of order 400(1190) km^3 sr w.e. acceptance, with a threshold of order 10^{17} eV or less. Clearly an accurate measure of the attenuation lengths is still an important factor in the design, but our goal here is to show that even conservative values for L_α give compelling results.

The simulation itself is a straightforward Monte Carlo integral of the acceptance, using an isotropic neutrino flux, and integrating through a shell-density model for the earth to determine the angular distribution of neutrinos that can interact within the detector. We use a 1:1:1 e:μ:τ mix of neutrino flavors, and include neutral and charged-current events. For the radio emission, the Zas-Alvarez-Muñiz parametrization [22] is used. Full vector polarization is implemented.

In Figs. 18 and 19, we show four views each of two different events with shower energies of 10^{18} and 10^{19} eV. Here the dots locate antenna nodes, and those that produce triggers are marked with an '+.' The incoming neutrino track is also indicated, with the shower occurring at its termination within the detector. The high refractive index of salt leads to a large Čerenkov angle of about 66° and accounts for the apparent "flatness" of the cone of triggered regions around the event vertices. These events are not selected to be typical but rather to illustrate the detector geometry. Events of lower energy, while able to be reconstructed via both event geometry and polarization information, are not as easily discerned by eye.
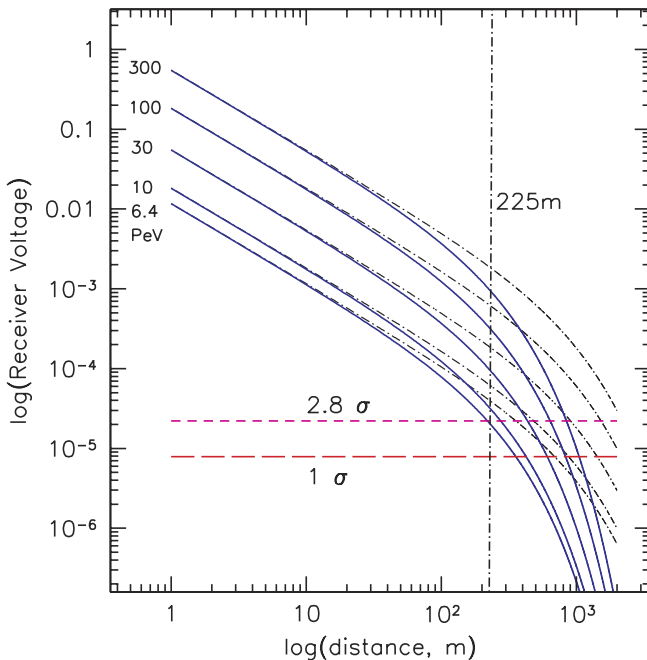

FIG. 17 (color online). Detection threshold estimates for a Salt dome Shower Array (SalSA). Solid & dash-dot curves show received voltages as a function of distance for a 250 m (solid) and 900 m (dash-dot) attenuation lengths, for the energies marked at left. The 1, 2.8σ noise levels shown are for a 450 K system temperature. The 225 m line is the antenna node spacing value used for the Monte Carlo.

1. Event angular resolution

We have studied the angular resolution possible with this realization of a SalSA. We used two different event types. First, a fully-contained event with a vertex near the center of the array was simulated; and second, an event with a vertex 250 m outside one of the array faces, with a shower direction parallel to the face (thus giving a partial intersection of the Čerenkov cone with the adjacent face) was

also simulated, both for a range of shower energies from $10^{16-19.5}$ eV. The simulation included thermal noise backgrounds and a 250 m salt attenuation length. Digital saturation (equivalent to a maximum of 10 bits of dynamic range) was also imposed on all signals to cap the available signal-to-noise ratio in a realistic way.

There are two stages to estimating the neutrino direction. First, the shower vertex must be determined. This task is largely separable from the estimation of the neutrino direction, since the constraints that determine vertex location by timing are far more rigid than constraints that arise from the observed amplitude. For example, pulse timing preci-
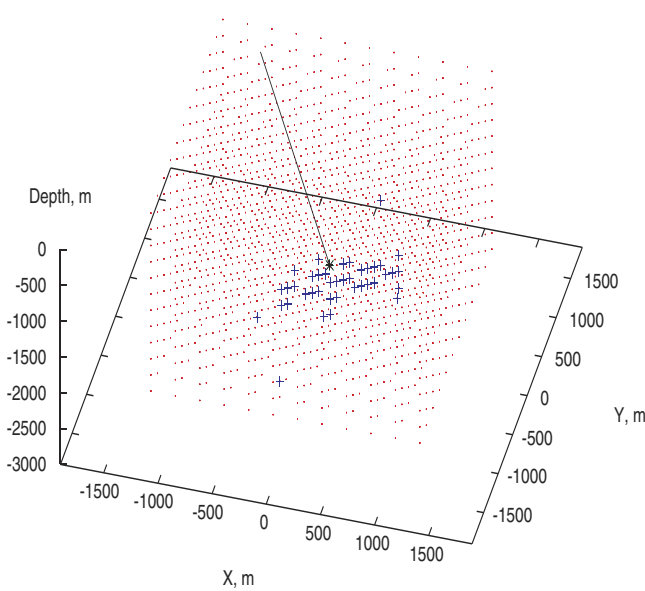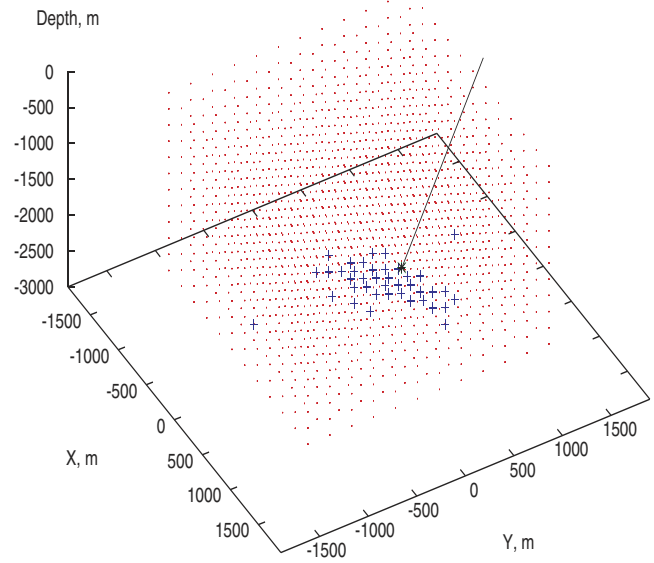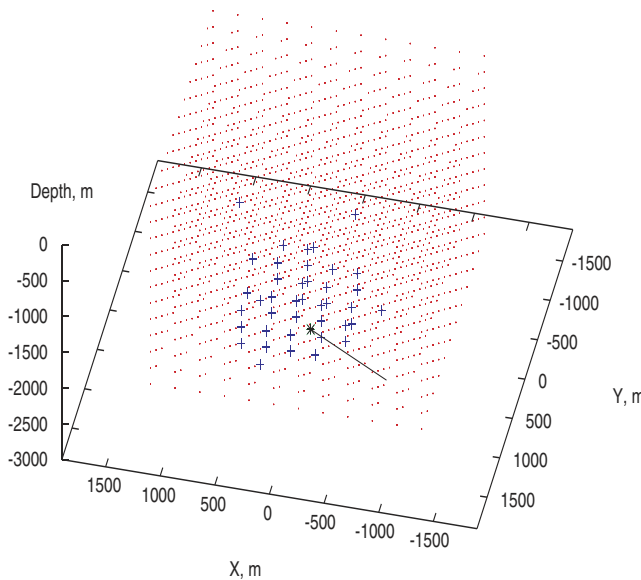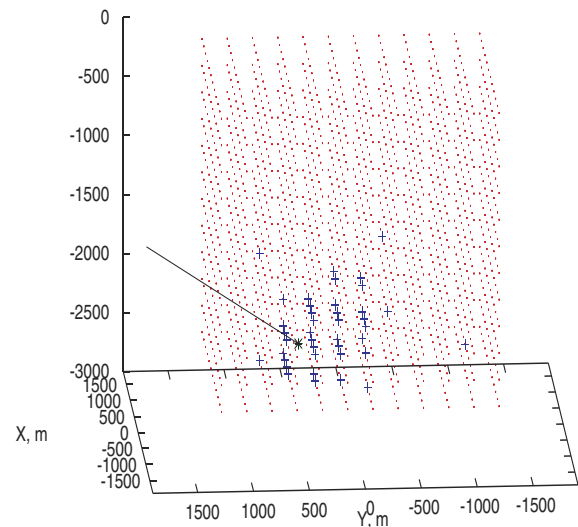

FIG. 18 (color online). Four views of the same 10^{18} eV hadronic shower, with directions in local altitude and azimuth (counterclockwise from east) shown. The dots mark antenna nodes, and crosses mark triggered nodes, with the incoming neutrino track shown up to its termination at the shower vertex.

sion for a node with a net SNR equivalent to about 4σ above the thermal noise level is of order $(4\Delta\nu)^{-1}$, or about 1.2 ns for the antenna parameters simulated here. In salt, this corresponds to a distance of 15 cm of light travel, and simple geometric triangulation for the trigger condition of five nodes on three different strings leads to precision on the vertex location of the same order, corresponding to arcminute-level precision on the angles. However, the uncertainty in the angles defining the vertex location only

indirectly affect the uncertainty in the estimated shower momentum vector.

The second stage in the reconstruction of neutrino direction is to use the vertex location determined by timing to estimate the field strength that would be observed by a given antenna for a given neutrino (and therefore shower) direction. At the energies of interest for neutrino charged and neutral current interactions, the estimated mean value of the Bjorken x variable, which primarily determines the
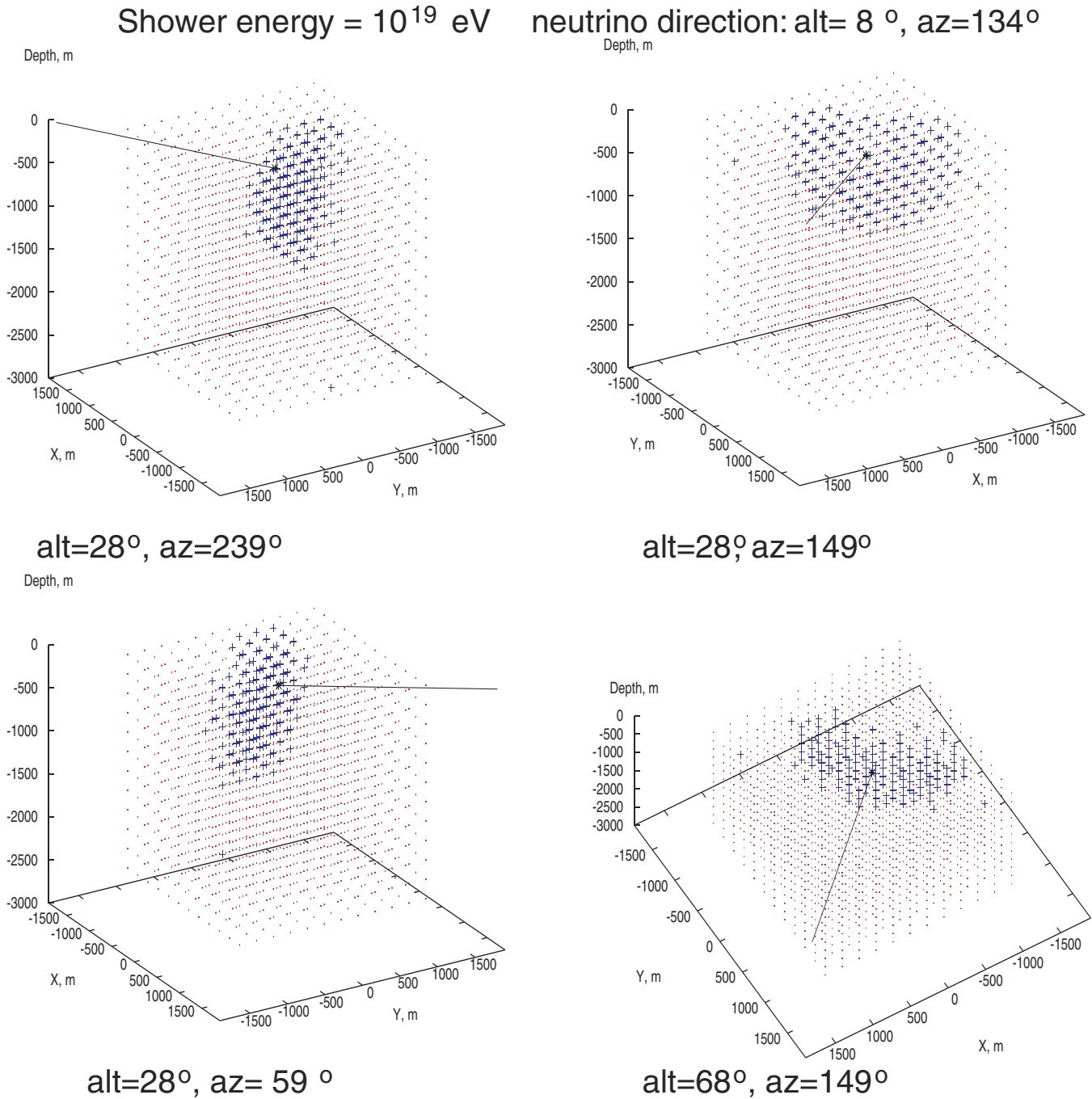

FIG. 19 (color online).   Similar to previous, with shower energy $E_{sh} = 10^{19}$ eV.

transverse momentum available to the shower, is of order 10^{-6} or less, and the shower momentum is thus highly aligned with the neutrino direction. Fitting of the shower direction is constrained by two characteristics of the Čerenkov radiation field from the shower: first, the amplitude of the field vs. polar angle around the shower direction, which is the classical Čerenkov cone, used in all ring-imaging Čerenkov detectors. The second characteristic is unique to radio Čerenkov ring imaging: the polarization of the radiation within the cone, which is also uniquely associated with the geometry of the shower.

In our studies here, we have concentrated on the second stage of the angle reconstruction, since the vertex reconstruction is common to all similar array detectors, and has been demonstrated in many examples. Systematics in the vertex reconstruction can of course eventually limit the angular resolution; we note this further in a later portion of this section.

The angular resolution capability was determined by a grid search over a χ^2 function based on field strength and polarization, for which all shower parameters but the angles were held fixed. The values of the parameters were determined by a quadratic fit to the local region around the χ^2 minimum. The χ^2 function itself is based on a model for the induced voltage at each antenna as a function of the parameterized pulse electric field strength $\mathbf{E}_i$ for the ith antenna:

$$R_i \mathbf{E}_i(\nu, E_{\mathrm{sh}}, \theta) = F(E_{\mathrm{sh}}, \nu) e^{-\ln(2)[(\theta_i - \theta_C)^2 / \Delta\theta^2]}$$
$$\times \hat{\mathbf{r}}_i \otimes (\hat{\mathbf{p}}_{\mathrm{sh}} \otimes \hat{\mathbf{r}}_i) \mathrm{V\ m^{-1}} \qquad (11)$$

where

$$F(E_{\mathrm{sh}}, \nu) = 2.53 \times 10^{-7} \frac{E_{\mathrm{sh}}}{1\ \mathrm{TeV}} \int_{\nu_{\min}}^{\nu_{\max}} \frac{\nu}{\nu_0} \frac{d\nu}{1 + (\nu/\nu_1)^{1.44}} \qquad (12)$$

Here the terms on the first line of Eq. (12) above are given by the parameterization of reference [31,32], with an additional frequency scaling terms ν_0, ν_1 to scale from ice to salt (see Appendix B). ν is the mean frequency for the antenna response, $\nu_{\min}$, $\nu_{\max}$ give the antenna bandwidth limits, R_i is the distance to the ith antenna, $\hat{\mathbf{r}}_i$ is a unit vector in that direction, and $\hat{\mathbf{p}}_{\mathrm{sh}}$ is a unit vector in the direction of the mean shower momentum vector. The latter terms determine the response to the linearly polarized Čerenkov emission, with the term $\hat{\mathbf{p}}_{\mathrm{sh}}$ containing explicitly the neutrino direction as described above (the $\otimes$ symbol here indicates a cross product).

For dipole antennas with effective height $\mathbf{h}$ that couple to electric field $\mathbf{E}$, the predicted induced voltage of the antenna into a matched load is given by

$$V_{i,\mathrm{dipole}} = \frac{1}{2} \mathbf{E}_i \cdot \mathbf{h}_i. \qquad (13)$$

Similarly, for our slot antennas which couple via the mag-

netic field components of the radiation $\mathbf{H}$, the induced voltage is determined by

$$V_{i,\mathrm{slot}} = \frac{1}{2} \mathbf{E}_i \otimes \mathbf{h}_i \qquad (14)$$

where $\mathbf{h}$ is aligned along the slot, with a magnitude determined by the maximum response of the antenna. The cross product then accounts for the magnetic coupling, which arises from the current loops around the slot, and gives maximum response for $\mathbf{E}$-vectors that are perpendicular to the slot axis at any azimuth. The resulting χ^2 function for all antennas is then

$$\chi^2 = \sum_{i=1}^{N_{\mathrm{ant}}} \frac{(V_{i,\mathrm{obs}} - V_i)^2}{2\sigma_i^2} \qquad (15)$$

where $V_{i,\mathrm{obs}}$ is the observed voltage for both slots and dipoles, and σ_i^2 is the variance of the noise, with $\sigma_i^2 = kT_{\mathrm{sys}} Z \Delta\nu$, for antenna and load impedance Z and system noise energy (including both receiver and ambient noise) kT_{sys}.
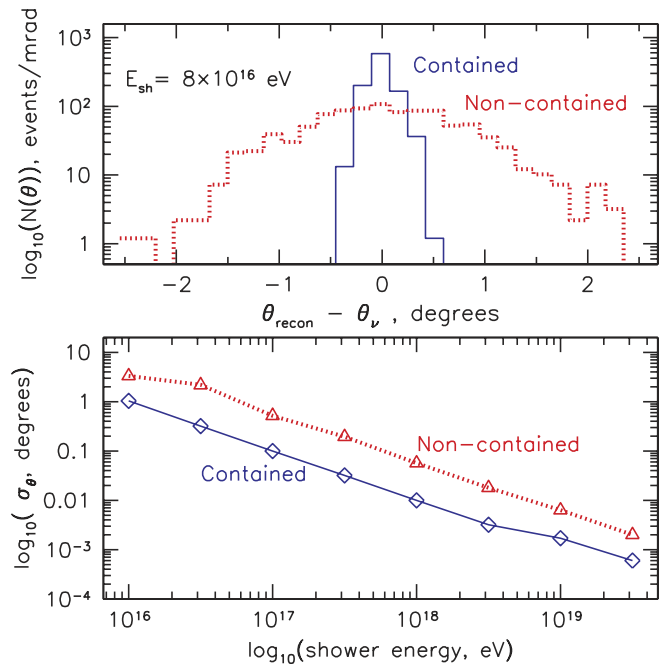

FIG. 20 (color online).   Simulation of the reconstructed angular resolution of the SalSA detector simulated here. Top: Examples of two reconstructed event angular distributions for a 8×10^{16} eV hadronic shower. The contained shower occurs near the center of the detector, and the noncontained shower occurs 250 m outside one of the faces, directed parallel to the face. Both showers were from horizontal neutrinos, and the reconstructed directions are for polar angle relative to the incident direction, estimated via the location of the minimum of χ^2, for 1000 trials for each shower type. Bottom: Standard deviations of angular distributions vs. shower energy, for the same shower types indicated in the top pane.

Figure 20 shows results from the study. In the top pane, the distribution of reconstructed angles for two event types at a fixed shower energy near the detector threshold are shown. The energy for these two events, 8×10^{16} eV, is typical of those expected for charged-current events giving hadronic showers with a mean inelasticity of order 0.25, for incoming neutrinos near the peak of the expected GZK neutrino distribution. Contained events, as expected, have much better angular resolution, with a standard deviation of about 0.15°, due to the much better constraints. Events for which the Čerenkov cone only partially intersects a face (in this case from a shower parallel to the face at a distance of 250 m outside the array) have degraded resolution, but still quite good, with a standard deviation of about 1°.

In the bottom pane of Fig. 20, the estimated angular resolution vs. shower energy is shown. There is a monotonic improvement with energy, as is expected because of the increase in the number of triggered nodes involved. It is likely that detector systematics, such as those related to vertex reconstruction, and systematic errors in the antenna positions, will begin to become important at reconstructed angles near the 1 arcminute level, though we have not yet investigated these in any detail. However, we note that the subarcminute angular resolution achieved here in the presence of what are mainly statistical errors in our simulation is not incommensurate with the additional strong constraints provided by the Čerenkov polarization information which is unique to this method.

2. Estimates of GZK neutrino event rates

To estimate event rates for different GZK neutrino models, our Monte Carlo is evaluated at discrete energies over the PeV to ZeV energy range, assuming a monoenergetic neutrino flux at each energy. The values of this function at discrete energies trace a smooth curve which represents a model-independent estimate of the sensitivity for fluxes which are smooth compared to the energy resolution of the instrument, which is of order $\Delta E/E \simeq 1$, limited primarily by the uncertainty in inelasticity, which has a mean of order 0.23 at these energies and a standard deviation about equal to its mean. The resulting curve gives the acceptance, in km^2 sr, which can be multiplied by the livetime to determine the exposure in km^2 sr s. The inverse of the exposure gives the model-independent flux sensitivity using the procedure outlined in Ref. [33].

Because the deployment of any large array as envisioned here proceeds in stages, we have chosen to simulate both the full array, and a 2×2 string array which would represent one of the initial core stages of deployment of the full array. This core array is on the same 225 m square grid as the full array, occupying the first 2×2 possible sites. Trigger conditions are the same as for the full array.

The result of these estimates for the flux sensitivity for 1 yr of exposure is shown in Fig. 21, plotted along with various estimates of GZK neutrino fluxes [5,34–36] for a

complete range of possible parameters. A model which just equaled the sensitivity curve for one decade of energy would give about 3 events. Also plotted is an earlier SalSA sensitivity estimate [37] with a simpler detector model and more conservative trigger but otherwise similar methodology. We have investigated the differences between these two results, and they can be understood in part as follows: the improved low-energy response of the current simulation appears to be due largely to the increase in antenna and string density over the earlier simulation, and the improved high-energy response for the previous simulation of Ref. [37] appears to be due to the fact that we have truncated the volume at a much smaller radius in our current simulation, and we are thus running out of salt around the periphery of the detector.

It is notable that even the sensitivity for the core 2×2 string array is adequate to begin to constrain almost all of
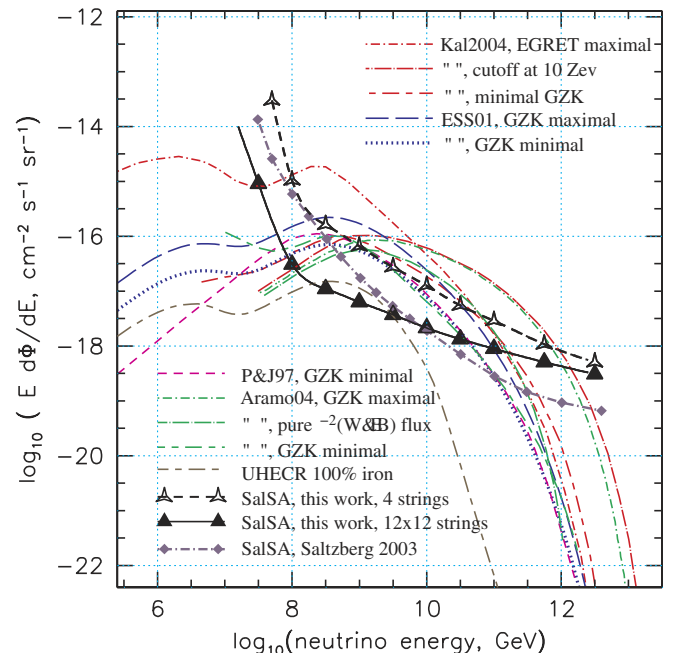

FIG. 21 (color online). Broad-spectrum flux sensitivity for a SalSA for 1 yr of exposure, estimated from a Monte Carlo simulation. A complete set of GZK models is shown, as well as an earlier estimate of SalSA sensitivity [37]. From the highest to lowest the legend indicates fluxes from Kalashev *et al.* (2002) [34] for the maximal level allowed by EGRET limits, an intermediate model with a 10 ZeV cutoff energy for the UHECR spectrum, and a minimal GZK model. The two models marked "ESS01" are from Engel *et al.* (2001) [5] for one minimal model and one with strong source evolution. The chosen P&J96 model [35] is for a minimal GZK flux. Three different models are shown from Aramo *et al.* (2005) [36], a maximal model subject only to observational constraints, an intermediate model which follows a pure E^{-2} spectrum as described by Ref. [39], and another minimal GZK model. Finally, a model based on the unlikely assumption that the UHECR composition is pure iron is shown [38].

the GZK neutrino models within 1 yr of operation. This may appear surprising, but it arises from the fact that events in the heart of the GZK energy range are well above the detection threshold for the array, and thus can trigger the detector from several e-folding distances of the salt attenuation length. Vertices for the events so detected are almost all well outside the array, so the angular resolution for reconstruction is much lower than for the full array, but as a discovery or GZK neutrino confirmation instrument, the relatively modest core array has great potential.

For GZK neutrino models we have included estimates from four independent calculations, and in several of these cases we provide both minimal and maximal estimates where they were made. Table II summarizes the event rates detected in our two SalSA configurations for the different GZK neutrino models shown in Fig. 21 per year of operation. For the three minimal GZK models shown the expected rates are about 21–28 events per year for the full array, and about a factor of 10 lower for the core array. If the observed rates are found to be significantly below this, the physics implications for both GZK neutrinos and cosmic rays would be serious as there are no currently self-consistent models which predict such low rates. One class of models in which the UHECR are predominantly heavy nuclei such as iron have been considered [38], and such models produce a somewhat lower GZK neutrino rate, leading to of order 3 events per year in our full array detector. The assumption of no light nuclei among the UHECR is however purely *ad hoc* at this stage, and the data do not support such an inference, but the importance of this study is that it demonstrates that there are no

currently known ways to evade the production of GZK neutrinos, even for assumed cosmic ray compositions that are artificially designed to do so.

GZK neutrino models in the midrange that assume stronger source evolution or a higher-energy cutoff to the cosmic ray source spectrum yield event SalSA rates in the range of 30-80 events per year in the full array. All of these models are still consistent with the Waxman-Bahcall limit for optically thin sources distributed cosmologically in a manner similar to AGN [39]. For the highest GZK neutrino models in which all parameters are maximized subject only to firm observational constraints such as the EGRET gamma-ray limits, the possible event rates are up to 280 per year.

We note that the event rates for the minimal GZK neutrino flux models, while still in the regime of small statistics, are likely to be measured with no physics background. The only possible background that we currently know of comes from charm quark production in ultra-high-energy cosmic rays, which can decay to energetic secondary muons, which can then shower via either bremsstrahlung or photonuclear processes in the detector. However, even the highest current estimates [40] for this process yield through going muon rates of ≤ 0.02 per year above 10^{17} eV over a 2.4 km radius area circumscribed around the detector volume. With regard to electromagnetic interference, even just several meters of overburden of rock or soil above a salt dome is enough to attenuate all anthropogenic radio or electronic interference, so that the system sensitivity will be subject only to the absolute thermal noise floor.

TABLE II. Event totals for various GZK neutrino models for 1 yr of operation for two SalSA configurations: a 2 by 2 string prototype array, and the full scale 144 string array which was the main focus of the simulations here. Both arrays were embedded within a 2 km radius salt volume, with 500 m overburden above the salt, and a 250 m salt attenuation length.

Model Reference	2×2 strings events/year	12×12 strings events/year
Minimal GZK models:		
Engel, Seckel, & Stanev 2000 [5]	2.4	21
Protheroe & Johnson 1996 [35]	2.9	27
Aramo *et al.* 2005 [36]	2.6	24
Models that saturate EGRET bound:		
Aramo *et al.* 2005 [36]	5.2	34
Kalashev *et al.* 2002 [34]	5.1	37
Models with strong source evolution:		
Engel, Seckel, & Stanev 2000 [5]	7.5	65
Aramo *et al.* 2005 [36]	15.3	80
Kalashev *et al.* 2002 [34]	16.8	90
Model that saturates all bounds:		
Kalashev *et al.* 2002 [34]	24.4	278
Model with Iron nuclei UHECR:		
Ave *et al.* 2005 [38]	0.4	3.4

For a system with a design lifetime of 10 years or more, even minimal GZK neutrino fluxes will produce a rich data sample of between several hundred and several thousand events, which would allow good precision on estimates of the GZK neutrino energy spectrum and sky distribution. Given that such neutrinos are directly coupled to the highest energy cosmic rays, for which the world sample is several dozen in 40 years of observation, the power of a SalSA array becomes clearly evident.

With regard to energy calibration of the events, we note the important possibility of measuring secondary showers from the energetic leptons in charged-current events compared to neutral current events would allow for full calorimetry of the neutral and charged-current channels, since at EeV energies, secondary leptons are very likely to shower at least 10% of their energy within 1–2 km. Landau-Pomeranchuk-Migdal effects on the development and radio emission pattern from electron-neutrino events [41] can potentially allow flavor identification, as can decays of tau leptons produced in tau neutrino events [42].

Dramatic increases in neutrino cross sections above the standard model, such as might be produced by the effects of microscopic black hole production in theories with large extra dimensions [43], would yield much larger event rates than described here; several thousand events per year are then possible even for minimal GZK models. Events so produced would also have quite distinct character compared to the dominant charge-current deep-inelastic neutrino events, since the decay of the black hole by Hawking radiation leads to a pure hadronic shower with no secondary high-energy leptons to produce more extended showers. There would also be no significant LPM effects in electron neutrinos, assuming the black hole production cross section dominated over the standard model cross sections. In fact, high cross sections combined with standard model GZK neutrino fluxes would serve to yield a detection with a proportionally smaller detector.

V. CONCLUSIONS

We conclude the following from our measurements and simulations:

(1) The Askaryan effect behaves as theoretically expected in measurements made in synthetic rock salt. Correlation of the strength of the radiation to the estimated charge excess is excellent.

(2) The polarization properties of the observed radio emission are consistent with coherent Čerenkov radiation, and can be used to derive geometric properties of the shower track to good precision.

(3) The observed radiation is completely coherent over many decades of shower energy, and a wide range of radio and microwave frequencies.

(4) Closely related transition radiation from the Askaryan charge excess of showers exiting dielec-

tric or metallic media has been measured and found to be in agreement with predictions.

(5) An antenna array of order 2.5 km on a side in an underground salt dome is well able to conclusively detect and characterize all current standard model GZK neutrino fluxes on even a 1 yr time scale; over 10 years of operation, good statistics can be obtained on the GZK neutrino spectrum above 10^{17} eV.

(6) Angular resolutions of $\leq 1°$ for noncontained, and several arcminutes or better for contained events can be expected for events in the GZK neutrino energy range.

APPENDIX A: DETAILS OF TRANSITION RADIATION ANALYSIS

The forward spectrum of transition radiation is given in [25] as

$$\frac{d^2 W_{TR}}{d\omega d\Omega} = \frac{h\alpha}{2\pi^3} \frac{\sqrt{\epsilon_2}\sin^2\theta\cos^2\theta}{1 - \beta^2\epsilon_2\cos^2\theta}|\zeta|^2 \qquad (A1)$$

where ζ is given by

$$\zeta = \frac{(\epsilon_2 - \epsilon_1)(1 - \beta^2\epsilon_2 - \beta\sqrt{\epsilon_1 - \epsilon_2\sin^2\theta})}{(\epsilon_1 + \sqrt{\epsilon_2}\sqrt{\epsilon_1 - \epsilon_2\sin^2\theta})(1 - \beta\sqrt{\epsilon_1 - \epsilon_2\sin^2\theta})} \qquad (A2)$$

ω is the bandwidth of the antenna ($d\omega = 2\pi d\nu$), and Ω is the solid angle subtended by the horn, given by $\Omega = A/d^2$ where d is the distance from the horn to the source and A is the area of the horn. θ is the angle between the beamline and the line to the horn. ϵ_1 and ϵ_2 are the upstream and downstream complex dielectric constants ($\epsilon_k = \epsilon'_k + i\epsilon''_k$), respectively. For these two experiments, the upstream medium is aluminum ($\epsilon'_1 \sim 10$) and the downstream medium is air ($\epsilon'_2 = (1.000\,35)^2$).

The energy is obtained by multiplying the right-hand side of Eq. (1) by the bandwidth and solid angle. To convert to power, divide the energy by the typical time of the pulse (about the inverse bandwidth of the antenna). The power

delivered to the load, P_L, is this power multiplied by the horn efficiency, about 0.5 [27].

It is useful to look at the electric field E as well as the power. The Poynting flux S is given by $S = P_L/A_{\text{eff}} = E^2/377$, where A_{eff} is the effective area of the antenna. Therefore $E = \sqrt{377 P_L/A_{\text{eff}}}$. We wish to look at the peak electric field, so we multiply E by a factor of $2\sqrt{2}$, since $E_{\text{peak}} = 2\sqrt{2} E_{\text{RMS}}$ for a perfectly triangular envelope.

The finite beam size introduces coherence corrections. The corrected power is given by

$$P = N_e(1 + N_e f_L f_T \chi) P_0 \qquad (A3)$$

where f_L, f_T, and χ are the longitudinal, transverse and angular form factors, respectively. If the distribution of the electrons is Gaussian, then Shibata *et al.* [44] give the form factors as:

$$f_L = \exp[-(\pi \sigma_L \cos\theta/\lambda)^2] \qquad (A4)$$

$$f_T = \exp[-(\pi \sigma_T \sin\theta/\lambda)^2] \qquad (A5)$$

$$\chi = \left(\frac{2\theta^2}{\pi\Omega^2} \int_0^{\pi/2\theta} x[(1-x)K(y) + (1 + x)E(y)]e^{(-\theta^2/\Omega^2)x^2} dx \right)^2 \qquad (A6)$$

where σ_L and σ_T are the longitudinal and transverse divergence parameters, Ω is the angular divergence parameter, and $K(y)$ and $E(y)$ are the complete elliptic integrals of the first and second kinds, where $y = 2\sqrt{x}/(1+x)$:

$$K(y) = \int_0^{\pi/2} (1 - y^2 \sin^2\omega)^{-1/2} d\omega \qquad (A7)$$

$$E(y) = \int_0^{\pi/2} (1 - y^2 \sin^2\omega)^{1/2} d\omega \qquad (A8)$$

In the perfectly coherent limit, $f_L = f_T = \chi = 1$ and since $N_e \gg 1$, $P = N_E^2 P_0$.

To compare the measured power to the calculated power, we take the average of V^2 over the measured pulse and divide by 50Ω. The measured voltage must be corrected for the attenuation in the circuit: $V_{\text{correct}} = V_{\text{meas}} 10^{\text{atten(dB)}/20}$.

To get the measured electric field, take the peak electric field $E_{\text{peak}} = 2V_{\text{peak}}/h_{\text{eff}}$ where h_{eff} is the effective height and V_{peak} is the measured peak voltage, with a factor of 2 to account for voltage division into a matched load.

APPENDIX B: DETAILS OF ČERENKOV RADIATION ANALYSIS

Zas, Halzen, and Stanev [24] provided a detailed analysis and simulations of coherent Čerenkov radio emission from high-energy showers in ice. A variety of studies since then have refined these initial results and extended them to various scenarios of neutrino flavor and energy [31,32]. For our analysis, we use the same approach as in our previous SLAC experiment [18], and adapt the parametrizations for the field strength produced by a shower in ice to the following form for salt:

$$R|\mathbf{E}(\nu, R, \theta_c)| = A_0 f_d \kappa \left(\frac{E_{\text{sh}}}{1 \text{ TeV}}\right) \frac{\nu}{\nu_0} \left(\frac{1}{1 + (\frac{\nu}{\nu_1})^\delta}\right) \qquad (B1)$$

where R is the distance from the charged-particle beam in Čerenkov cone direction. A_0 and δ are empirically determined coefficients, $A_0 = 2.53 \times 10^{-7}$ and $\delta = 1.44$. The factor f_d is a scaling factor for the difference of radiation length and density between salt and ice, $f_d = 0.52$, and $\kappa \approx 0.5$ is a factor accounting for antenna near-field effects, with an estimated systematic uncertainty of $\sim 30\%$. Here E_{sh} is the shower energy and is given by $E_{sh} = E_e N_e t$, where $E_e = 28.5$ GeV is the energy of the electrons in the beam, N_e is the number of electrons and t is the thickness of the radiator in X_0. The parameters $\nu_0 = 1100$ MHz, and $\nu_1 = 2680$ MHz determine the decoherence behavior, and are estimated from the parameters for ice, scaled by the ratio of the radiation length in ice and salt, calculated from the empirical formula:

$$X_0 = 716.4 \frac{\sum_i A_i}{\sum_i (Z_i(Z_i + 1) \ln\frac{287}{\sqrt{Z_i}})} \left[\frac{\text{g}}{\text{cm}^2}\right] \qquad (B2)$$

where Z_i is the atomic number and A_i is the atomic weight of the elements which form the molecule.

[1] F. Halzen, R. J. Protheroe, T. Stanev, and H. P. Vankov, Phys. Rev. D **41**, 342 (1990); J. Wdowczyk and A. W. Wolfendale, Astrophys. J. **349**, 35 (1990).

[2] K. Greisen, Phys. Rev. Lett., **16**, 748 (1966).

[3] G. T. Zatsepin and V. A. Kuzmin, Pis'ma Zh. Eksp. Teor. Fiz. **4**, 114 (1966) [JETP Lett. **4**, 78 (1966)].

[4] V. S. Berezinsky and G. T. Zatsepin, Phys. Lett. B **28**, 423 (1969); Sov. J. Nucl. Phys. **11**, 111 (1970); F. W. Stecker, Astrophys. Space Sci. **20**, 47 (1973); F. W. Stecker, Astrophys. J. **228**, 919 (1979).

[5] R. Engel, D. Seckel, and T. Stanev, Phys. Rev. D **64**, 093010 (2001).

[6] D. Seckel and G. Frichter, *Proceedings of the 1st International Workshop on Radio Detectection High Energy Particles (RADHEP 2000)*, edited by Saltzberg and Gorham (AIP, New York, 2001).

[7] G. A. Askaryan, JETP Lett. **14**, 441 (1962).

[8] G. A. Askaryan, JETP Lett. **21**, 658 (1965).

[9] I. Kravchenko *et al.*, Astropart. Phys. **20**, 195 (2003).

[10] P. Miocinovic *et al.*, astro-ph/0503304; A. Silvestri *et al.*, astro-ph/0411007; http://www.phys.hawaii.edu/~anita

[11] N. G. Lehtinen, P. . Gorham, A. R. Jacobson, and R. A. Roussel-Dupŕe, Phys. Rev. D **69**, 013008 (2004).

[12] I. M. Zheleznykh, in *Proceedings of Neutrino 1988*, edited by J. Schneps (World Scientific, Singapore, 1989).

[13] R. D. Dagkesamanskii and I. M. Zheleznykh, JETP Lett. **50**, 233 (1989).

[14] T. H. Hankins, R. D. Ekers, and J. D. O'Sullivan, Mon. Not. R. Astron. Soc. **283**, 1027 (1996).

[15] P. W. Gorham *et al.*, Phys. Rev. Lett. **93**, 041101 (2004).

[16] M. Chiba, T. Kamijo, O. Yasuda *et al.*, Phys. At. Nucl. **67**, 2050 (2004).

[17] P. Gorham, D. Saltzberg, A. Odian *et al.*, Nucl. Instrum. Methods Phys. Res., Sect. A **490**, 476 (2002).

[18] D. Saltzberg, P. Gorham, D. Walz *et al.*, Phys. Rev. Lett., **86**, 2802 (2001).

[19] K. Kamata, and J. Nishimura, Suppl. Prog. Theor. Phys. **6**, 93 (1958); K. Greisen, in *Progress in Cosmic Ray Physics*, edited by J. G. Wilson (North Holland, Amsterdam, 1965), Vol. III, p. 1.

[20] *Dielectric Materials and Applications*, edited by A. von Hippel (Artech House, Boston, 1995).

[21] W. R. Nelson, H. Hirayama, and D. W. O. Rogers, SLAC-265, Stanford Linear Accelerator Center, 1985, see also http://www.slac.stanford.edu/egs/.

[22] J. Alvarez-Muñiz and E. Zas, Phys. Lett. B, **411**, 218 (1997).

[23] J. Alvarez-Muñiz and E. Zas Phys. Lett. B **434**, 396 (1998).

[24] E. Zas, F. Halzen, and T. Stanev, Phys. Rev. D **45**, 362 (1992).

[25] P. W. Gorham, D. P. Saltzberg, P. Schoessow et al. Phys. Rev. E **62**, 8590 (2000).

[26] D. Williams, unpublished dissertation, UCLA, 2003.

[27] J. D. Kraus, *Antennas*, (McGraw-Hill, New York, 1988).

[28] G. Varner, P. Gorham, and J. Cao, in *Proceedings of SPIE conference 4858, Particle Astrophysics Instrumentation*, edited by P. Gorham (SPIE, Bellingham, WA, 2003), p. 285.

[29] G. Varner *et al.*, University of Hawaii internal report (2004), http://www.phys.hawaii.edu/ idlab/project_files/salt/docs/GEISER_wu_2.0.pdf

[30] R. Gandhi, Nucl. Phys. B Proc. Suppl. **91**, 453 (2001).

[31] J. Alvarez-Muñiz, R. A. Vázquez, and E. Zas, Phys. Rev. D **62** 063001, (2000).

[32] J. Alvarez-Muñiz, R. A. Vázquez, and E. Zas Phys. Rev. D **61**, 023001 (2000).

[33] L. A. Anchordoqui, J. L. Feng, H. Goldberg, and A. D. Shapere, Phys. Rev. D **66**, 103002 (2002).

[34] O. E. Kalashev, V. A. Kuzmin, D. V. Semikoz, and G. Sigl, Phys. Rev. D **66**, 063004 (2002).

[35] R. J. Protheroe and P. A. Johnson, Astropart. Phys. **4**, 253 (1996).

[36] C. Aramo *et al.*, Astropart. Phys. **23**, 65 (2005).

[37] D. Saltzberg *et al.*, *Proceedings of SPIE conference 4858, Particle Astrophysics Instrumentation*, edited by P. Gorham (SPIE, Bellingham, WA, 2003),p. 191.

[38] M. Ave, N. Busca, A. V. Olinto, A. A. Watson, and T. Yamamoto, Astropart. Phys. **23**, 19 (2005).

[39] E. Waxman and J. Bahcall, Phys. Rev. D **59**, 023002 (1999).

[40] A. Misaki *et al.*, Proceedings of the 26th ICRC, University of Utah, 1999, (unpublished).

[41] J. Alvarez-Muñiz, R. A. Vázquez, and E. Zas, Phys. Rev. D **61**, 023001 (2000).

[42] J. G. Learned and S. Pakvasa, Astropart. Phys. **3**, 267 (1995).

[43] J. L. Feng and A. D. Shapere, Phys. Rev. Lett. **88**, 021303 (2002); J. Alvarez-Muniz, J. L. Feng, F. Halzen, T. Han, and D. Hooper, Phys. Rev. D **65**, 124015 (2002).

[44] T. Takahashi, Y. Shibata, K. Ishi *et al.*, Phys. Rev. E **62**, 8606 (2000).